Geophysical Journal International

Geophys. J. Int. (2024) **239,** 1038–1062
Advance Access publication 2024 August 30
GJI Seismology

https://doi.org/10.1093/gji/ggae315

Effects of 2.5-D ultra-low and ultra-high velocity zones on flip-reverse-stacking (FRS) of the ScS wavefield

Michael S. Thorne [1], Surya Pachhai [1] and Edward J. Garnero [2]

[1] *Department of Geology & Geophysics, University of Utah, Salt Lake City, UT* 84112*, United States. E-mail: michael.thorne@utah.edu*
[2] *School of Earth and Space Exploration, Arizona State University, Tempe, AZ* 85287*, United States*

Accepted 2024 August 29. Received 2024 August 28; in original form 2024 July 8

SUMMARY

Within the last decade, thin ultra-low velocity zone (ULVZ) layering, sitting directly on top of the core–mantle boundary (CMB), has begun to be investigated using the flip-reverse-stack (FRS) method. In this method, pre- and post-cursor arrivals that are symmetrical in time about the ScS arrival, but with opposite polarities, are stacked. This same methodology has also been applied to high velocity layering, with indications that ultra-high velocity zones (UHVZs) may also exist. Thus far, studies using the FRS technique have relied on 1-D synthetic predictions to infer material properties of ULVZs. 1-D ULVZ models predominantly show a SdS precursor that reflects off the top of the ULVZ and an ScscS reverberation within the ULVZ that arrives as a post-cursor. 1-D UHVZ models are more complex and have a different number of arrivals depending on a variety of factors including UHVZ thickness, velocity contrast, and lateral extent. 1-D modelling approaches assume that lower mantle heterogeneity is constant and continuous everywhere across the lower mantle. However, lower mantle features display lateral heterogeneity and are either finite in extent or display local thickness variations. We examine the interaction of the ScS wavefield with ULVZs and UHVZs in 2.5-D geometries of finite extent. We show that multiple additional arrivals exist that are not present in 1-D predictions. In particular, multipath ScS arrivals as well as additional post-cursor arrivals are generated. Subsequent processing by the FRS method generates complicated FRS traces with multiple peaks. Furthermore, post-cursor arrivals can be generated even when the ScS ray path does not directly strike the heterogeneity from above. Analysing these predictions for 2.5-D models using 1-D modelling techniques demonstrates that a cautious approach must be adopted in utilization and interpretation of FRS traces to determine if the ScS wavefield is interacting with a ULVZ or UHVZ through a direct strike on the top of the feature. In particular, traveltime delays or advances of the ScS arrival should be documented and symmetrical opposite polarity arrivals should be demonstrated to exist around ScS. The latter can be quantified by calculation of a time domain multiplication trace. Because multiple post-cursor arrivals are generated by finite length heterogeneities, interpretation should be confined to single layer models rather than to interpret the additional peaks as internal layering. Furthermore, strong trade-offs exist between *S*-wave velocity perturbation and thickness making estimations of ULVZ or UHVZ elastic parameters highly uncertain. We test our analysis methods using data from an event occurring in the Fiji-Tonga region recorded in North America. The ScS bounce points for this event sample the CMB region to the southeast of Hawaii, in a region where ULVZs have been identified in several recent studies. We see additional evidence for a ULVZ in this region centred at 14°N and 153°W with a lateral scale of at least 250 km × 360 km. Assuming a constant *S*-wave velocity decrease of −10 or −20 per cent with respect to the PREM model implies a ULVZ thickness of up to 16 or 9 km, respectively.

Key words: Composition and structure of the mantle; Core–mantle boundary; Body waves; Seismic discontinuities.

1 INTRODUCTION

The largest absolute density contrast anywhere on Earth occurs at the core–mantle boundary (CMB) making it a natural place for heterogeneous materials to accumulate. Anomalous CMB materials are potentially detectable with seismic imaging, which has revealed a wide variety of possible features in past investigations. Decades of research has revealed extreme seismic velocity reductions at the CMB. The majority of these studies identify what are called ultra-low velocity zones (ULVZs, see recent review in Yu & Garnero 2018). ULVZs are reported to have thicknesses up to a few tens of km and velocity reductions of a few tens of per cent with respect to standard reference earth models, for example PREM (Dziewonski & Anderson 1981). A number of studies have demonstrated that data are better fit by ULVZ models with elevated density, for example up to 10 per cent denser than the surrounding mantle (e.g. Rost *et al.* 2005; Brown *et al.* 2015), though density is typically more difficult to constrain.

Deciphering the origin, dynamics and structural details of ULVZs may be key to understanding a number of lower mantle features, such as Large Low Velocity Provinces (LLVPs, McNamara 2019), deep mantle plumes (Jones *et al.* 2019; Dannberg *et al.* 2021), as well as deeply subducted former basaltic oceanic crust (Andrault *et al.* 2014; Pradhan *et al.* 2015; Li 2023). ULVZs thus may link to important ongoing geodynamic processes (see review in McNamara 2019). Yet ULVZ origin, composition and dynamic consequences are still debated. For example, a wide variety of mechanisms have been proposed to generate ULVZs. Some of the most common mechanisms invoked are that they may arise through partial melting of some deep mantle component. One possibility is that of some mineralogical component of downwelling subducted slabs (e.g. Andrault *et al.* 2014; Pradhan *et al.* 2015; Thorne *et al.* 2019; Festin *et al.* 2024; Wolf *et al.* 2024). Partial melting may be most feasible in the highest temperature regimes of the lowermost mantle, such as at the margins or in the interiors of LLVPs (Li *et al.* 2017), or from thermal boundary layer instabilities generated at the front of a subducted slab encountering the CMB (Tan *et al.* 2002), or from hot thermal ridges at the CMB, between downwelling and upwelling flow regions (Li 2020). If compositionally distinct, ULVZ material may be related to products from core–mantle interactions (e.g. Manga & Jeanloz 1996; Garnero & Jeanloz 2000; Mao *et al.* 2006; Otsuka & Karato 2012), subducted oceanic crust (Ko *et al.* 2022), or possibly remnants from an ancient basal magma ocean (e.g. Labrosse *et al.* 2007; Nomura *et al.* 2011; Pachhai *et al.* 2022a). All these possibilities may be at play, both collectively and independently, in the creation of seismically detectable ULVZ anomalies. This raises the possibility that ULVZs may be widespread, even ubiquitous, along the CMB (Thorne *et al.* 2021; Hansen *et al.* 2023). In order to explain the seismic observations, these proposed processes must have in common the creation of intrinsically dense material with reduced *P*- and *S*-wave seismic velocities.

Geodynamic simulations demonstrate that dense ULVZs will advect towards regions of mantle upwelling; this includes the margins of compositionally distinct LLVPs or the hottest centres of solely thermal-origin LLVPs (Li *et al.* 2017). Indeed, ULVZs appear to preferentially concentrate near LLVP boundaries (Yu & Garnero 2018; Sun *et al.* 2019; Jenkins *et al.* 2021; Lai *et al.* 2022; Li *et al.* 2022). However, they have also been mapped in regions far from LLVPs, such as those beneath long histories of subduction (Havens & Revenaugh 2001; Thorne *et al.* 2019; Thorne *et al.* 2020, 2021; Festin *et al.* 2024; Wolf *et al.* 2024). ULVZs are also found beneath surface locations of hot spot volcanoes (e.g. Helmberger *et al.* 1998; Williams *et al.* 1998; Cottaar & Romanowicz 2012; Yuan & Romanowicz 2017; Kim *et al.* 2020; Krier *et al.* 2021; Cottaar *et al.* 2022). Detecting ULVZs in such diverse dynamic regimes, that is from putative downwelling to upwelling locations may relate to their formation (downwelling) and resting place (upwelling) locations. If ULVZs were solely created as primordial materials (e.g. Labrosse *et al.* 2007), they would have long since advected to their final resting spots either at LLVP boundaries or beneath whole mantle plumes (if dense and stable) and not be found beneath subduction. The possibility of widespread ULVZs (Thorne *et al.* 2021; Hansen *et al.* 2023), in contrast, would involve a near constant replenishing from subducted materials, CMB reaction products or both.

Seismic studies of fine-scale CMB layering has predominantly presented strong velocity reductions. Some recent investigations, however, have explored the possibility of thin high velocity layering at the CMB (Fan *et al.* 2022), with some suggestion of ultra-high velocity zones (UHVZs, Garnero *et al.* 2020; Yu 2020). UHVZs are an order of magnitude thinner than the 200–300 km thick D'' discontinuity associated with the post-perovskite phase transition in cooler than average regions, such as the circum-Pacific (e.g. Cobden *et al.* 2015; Whittaker *et al.* 2016; Borgeaud *et al.* 2017; Li *et al.* 2021). We note the UHVZs are distinct from alternatives to the ULVZ previously presented that require velocity reductions in the layer, such as core rigidity zones or core–mantle transition zones (Buffett *et al.* 2000; Garnero & Jeanloz 2000; Rost & Revenaugh 2001).

Detection of thin high velocity zones at the CMB may be inherently more difficult to detect than low velocity zones. ULVZs are routinely detected from waveform anomalies of the SPdKS seismic phase, but SPdKS waveforms are less perturbed by high velocity structures (Pachhai *et al.* 2022b). Many studies suggest that small-scale high velocity anomalies in the lower mantle may exist from observations of PKP scattering. These scatterers are often explained as possible remnants of subducted slabs (e.g. Ma *et al.* 2016; Mancinelli *et al.* 2016; Frost *et al.* 2017; Haugland *et al.* 2018). There are additionally potential core–mantle reactions that could generate thin regions with high seismic velocity anomalies at the CMB (Ko *et al.* 2022).

Core reflected seismic phases have been exceedingly useful in detecting and modelling fine-scale CMB layering (e.g. ULVZs) and their elastic parameters. In particular, ScP and PcP arrivals have been used extensively, particularly at relatively high frequency (e.g. around 1 Hz). The ScP arrival (an *S* wave that reflects off of the CMB and converts to a *P* wave) has been used in dozens of studies to detect and analyse ULVZ layering (e.g. Garnero & Vidale 1999; Rost & Revenaugh 2003; Pachhai *et al.* 2014; Hansen *et al.* 2023; Pachhai *et al.* 2023). The PcP arrival (a core reflected *P*-wave arrival) has also been used, but to a much lesser extent (e.g. Thybo *et al.* 2003; Rost & Thomas 2010; Gassner *et al.* 2015). More recently a variety of studies have begun to utilize broadband transverse component ScS arrivals (e.g. Lay *et al.* 2006; Avants *et al.* 2006a, b; He & Wen 2009). The PcS arrival has not been used in any previous studies.

A key aspect of using any core-reflected arrivals for imaging CMB layering is that when they interact with layered structure above the CMB, pre- and post-cursor arrivals are generated that are sensitive to layer thickness and material elastic parameters. Pre- and post-cursor arrivals associated with ScP, PcP and ScS are all low amplitude arrivals with precursor arrivals for ScP and PcP especially difficult to distinguish above seismic noise levels. Analysis of ScP and PcP arrivals are thus typically accomplished by stacking the data through different array processing techniques. For example, these

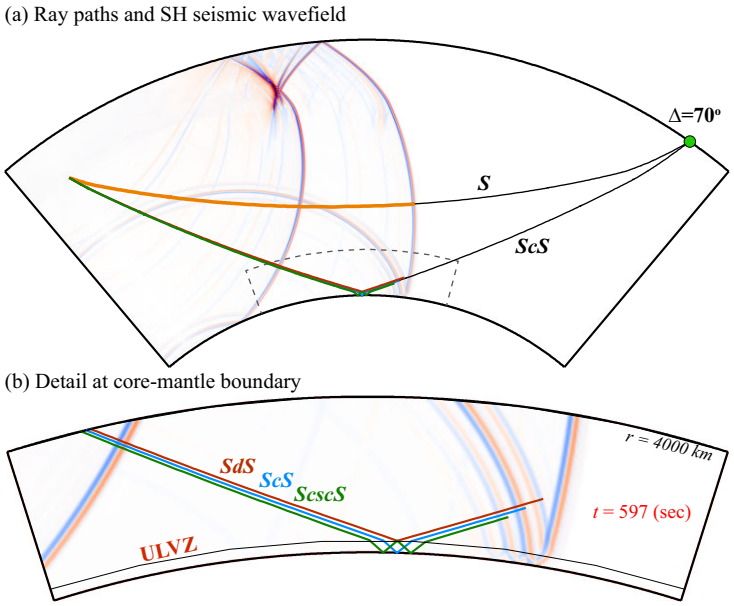

Figure 1. (a) Ray paths for direct S and ScS arrivals are drawn in black for a receiver at a distance of 70°. Ray paths for direct *S* wave (orange), ScS (blue), SdS (red) and ScscS (green) are drawn at $t = 597$ s. (b) Detailed view of panel (a), within the box defined by dashed lines, near the CMB. The solid line is drawn in at the top of the ULVZ ($h = 40$ km and $\delta V_S = -20$ per cent). Background shows the SH-velocity wavefield at a time of 597 s for a 500 km deep event with a dominant source period of 5 s. Ray paths and waveform calculations are for the ULVZ model. Non-linear scaling is applied to wavefield amplitudes to highlight lower amplitude arrivals. An animation of the ray paths and wavefield is given in supplementary online materials Movie_S1.mp4.

types of signals are well-suited to be studies with seismic arrays from the International Monitoring System (e.g. Rost & Thomas 2009). Stacking seismograms gives a $\sqrt{N}$ improvement on signal-to-noise ratio (SNR), where N is the number of seismograms in the stack (Robinson 1970). It was noted in Zhao *et al.* (2017), that when the ScS arrival interacts with a laterally homogeneous ULVZ, the pre- and post-cursor arrivals are nearly symmetric in time about the ScS arrival but opposite in polarity. Ray paths for a ULVZ structure are shown in Fig. 1, for ScS, the precursor SdS (the reflection off of the top of the ULVZ), and the post-cursor ScscS (a reverberation within the ULVZ). The seismic wavefield at one instance in time ($t = 597$ s) is also shown. Here we note that the CMB reflection wave front that is out in front (the precursor SdS—red ray path) is first blue and then red. But the next two consecutive CMB arrivals (ScS—blue ray path) and (ScscS—green ray path) have the opposite polarity—the wave front is first red and then blue. This opposite polarity behaviour led to the flip-reverse-stack (FRS) method (Zhao *et al.* 2017). The process is illustrated in Fig. 2 for a variety of synthetic models for both low (ULVZ) and high (UHVZ) velocity CMB layering. Consider the bottom trace of Fig. 2(a). This trace was computed for a 1-D ULVZ model with a thickness of $h = 20$ km, and *S*-wave velocity reduction (δV_S) of 20 per cent with respect to PREM. Here we split the trace into two parts, with the precursory and post-cursory parts in blue and red—corresponding to before and after the peak of the ScS arrival, respectively. If we time-reverse the blue portion of the waveform, shift it in time to start when the red portion starts (thus, overlay it on the red portion, see Fig. 2b), then the pre- and post-cursor arrivals occur at approximately the same time, but with opposite polarities. Thus, flipping the precursory blue trace and then adding it to the red trace results in the symmetric ScS arrival cancelling out. A single trace with a peak at the time of the summed pre- and post-cursor remains, which we refer to as S^U (Fig. 2c). Because we have doubled the number of traces going into the stack, we have improved the SNR by a factor of $\sqrt{2N}$.

This FRS technique has been used in a number of studies to detect ULVZ structure (Zhao *et al.* 2017; Fan & Sun 2021; Jenkins *et al.* 2021; Fan *et al.* 2022) and in one study to infer thin high velocity structure (Fan *et al.* 2022). When using the FRS technique, all of these studies used 1-D waveform modelling or ray tracing to infer layer existence and properties. But recent 2-D and 2.5-D waveform modelling efforts have shown that core reflected arrivals like ScP and ScS have additional arrivals, beyond the 1-D pre- and post-cursors arrivals, when the ULVZs have finite lengths (Brown *et al.* 2015; Lai *et al.* 2022; Pachhai *et al.* 2023). In the case of ScP, some of these additional arrivals can constructively/destructively interfere with ScP post-cursors traditionally used to infer ULVZ parameters. Using high frequency 2.5-D synthetic modelling Pachhai *et al.* (2024) identified two new ScP post-cursor arrivals (called Sl_1P and Sl_2P) that arise from the ULVZ lateral boundaries. Depending on the ULVZ location, these additional post-cursors can be generated even when the ScP bounce point is outside of the ULVZ. These post-cursors can have similar arrival time and amplitude as post-cursors generated by 1-D ULVZ models and thus may be misinterpreted as a reflection off the top of a 1-D ULVZ model, which also can lead to misinterpretation of ULVZ parameters and thickness. Evidence that these additional post-cursor arrivals are observable in real data is shown in Pachhai *et al.* (2023).

In this paper, we further investigate the nature of ScS pre- and post-cursor arrivals in 2.5-D heterogeneous media (see e.g. Jahnke *et al.* 2008). Here we make synthetic predictions in the presence of both low and high velocity layering with finite extent, where the model is defined on a 2-D grid. As discussed in the next section, this model is virtually rotated around an axis passing through the source and centre of the Earth creating an axi-symmetric model. As this generates the correct geometric spreading in 3-D it is considered hybrid between a 2-D and 3-D method and referred to as a 2.5-D method. We examine what arrivals are present in the 2.5-D synthetics that are not present in 1-D predictions, and how these

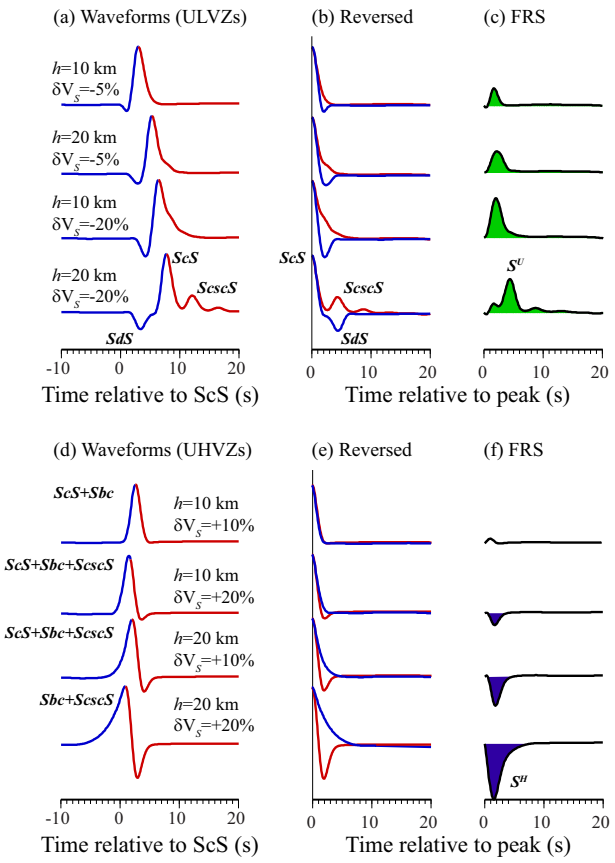

Figure 2. (a) Transverse component displacement waveforms for four ULVZ models. Traces are separately coloured blue and red on either side of the ScS peak. Traveltimes are plotted relative to the PREM predicted ScS arrival time. (b) The waveforms shown in panel (a) have the blue portion of the wavefield reversed in time and overlain on the red portion. (c) Now if one flips the blue portion from (b) and adds it to the red portion, you get the flip-reverse-stack (FRS) trace as shown in black with positive amplitudes shaded green. (d) same as in (a) but for four models of ultra-high velocity zones. (e) and (f) the same as (b) and (c) except for the UHVZ models. The thickness and *S*-wave velocity contrast of the model is shown next to each waveform in panels (a) and (d). Waveforms are shown for an epicentral distance of 70°.

arrivals affect the ability to retrieve ULVZ and UHVZ parameters using the FRS method. We examine data previously investigated in Zhao *et al.* (2017) in the eastern Pacific Ocean region that demonstrates that ULVZs may be reliably detected using the FRS method.

2 SYNTHETIC ANALYSIS METHODS

In order to assess how well the FRS method works under the conditions of finite length ULVZ and UHVZ models, we compute synthetic predictions using the SHaxi finite difference method. SHaxi is an axisymmetric method that computes the full seismic wavefield for models on a 2-D grid rotated around an axis passing through the source and the centre of the Earth (Jahnke *et al.* 2008). The method has been used in a wide variety of deep Earth studies (e.g. Thorne *et al.* 2007, 2013a; Yao *et al.* 2015). In this study we compute synthetic seismograms with 5 s dominant periods and a 500 km source depth.

We consider four classes of models for both ULVZs and UHVZs as summarized in Table 1. Specifically, we characterize the heterogeneity as either being thin ($h = 10$ km) or thick ($h = 20$ km) and having either a weak (-5 per cent for ULVZs and $+10$ per cent for UHVZs) or strong (-20 per cent for ULVZs and $+20$ per cent for UHVZs) velocity perturbation. Definitions for ULVZ and UHVZ geometric parameters are given in Fig. 3(e) where the source is located at an angular distance of 0°. The near edge of the ULVZ or UHVZ is given by l_1 and the far edge is given by l_2. The length of the heterogeneity in the great circle arc distance is given by l. We compute models with three different lengths on the CMB of $l = 3°$, 6°, or 12°, and 26 different edge positions from $l_1 = 20°$ to 45° in 1° increments. In these experiments, we do not vary the density contrast but fix it at $+5$ per cent, which is a reasonable choice for ULVZ models from previous results (e.g. Rost *et al.* 2006; Brown *et al.* 2015). It is unknown what density contrasts may be reasonable for UHVZs, so we use the $+5$ per cent contrast for those models as well. This gives us a total of 252 ULVZ and 252 UHVZ models to test. These synthetic predictions are treated as real observations, for which we can test 1-D waveform fitting approaches to assess parameter recovery. In order to facilitate discussion of our results, we will generalize our discussion based on the spatial relationship between ULVZ and ScS bounce point on the CMB as shown in Fig. 3. For simplicity we only discuss results for epicentral distances of 70°. At this distance, for a 500 km source depth, the ScS bounce point occurs at an angular distance of 34.1° from the earthquake source. Variations in arrival amplitudes and phase exist as a function of both epicentral distance and source depth. But we only discuss this single distance and depth as our goal is to demonstrate the primary differences between 1-D and 2.5-D model predictions and to gain insight into when the 1-D waveform fitting approaches are applicable. We chose 70° as a representative distance as ScS is well-separated from the direct *S*-wave arrival in order to investigate precursory arrivals.

We test how well the 1-D waveform modelling method of Zhao *et al.* (2017) is capable of recovering correct ULVZ and UHVZ parameters from the 2.5-D synthetic models. This method is also used in other studies (Fan & Sun 2021; Fan *et al.* 2022) and is ultimately

Table 1. Model space.

Heterogeneity	Type	h (km)	δV_S (per cent)	l (°)	l_1 (°)[a]
ULVZ	Thin/weak	10	–5	3°, 6°, 12°	20°–45°
ULVZ	Thick/weak	20	–5	3°, 6°, 12°	20°–45°
ULVZ	Thin/strong	10	–20	3°, 6°, 12°	20°–45°
ULVZ	Thick/strong	20	–20	3°, 6°, 12°	20°–45°
UHVZ	Thin/weak	10	+10	3°, 6°, 12°	20°–45°
UHVZ	Thick/weak	20	+10	3°, 6°, 12°	20°–45°
UHVZ	Thin/strong	10	+20	3°, 6°, 12°	20°–45°
UHVZ	Thick/strong	20	+20	3°, 6°, 12°	20°–45°

[a]Models computed with edge locations from 20° to 45° in 1° increments.

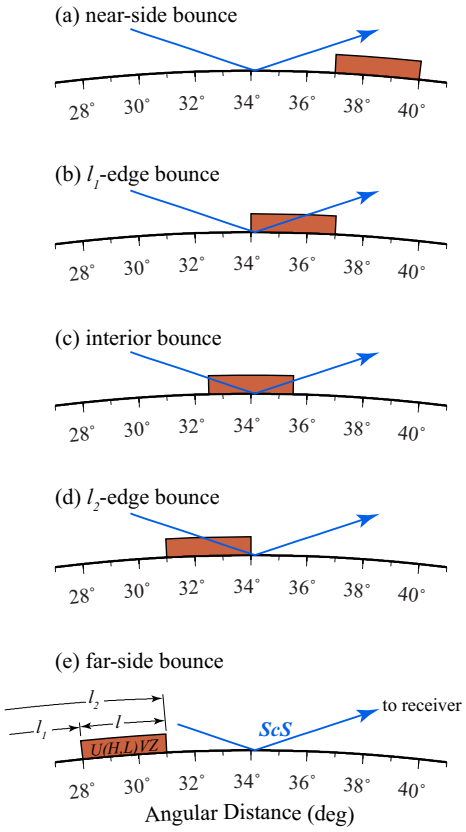

Figure 3. For a 500 km deep source at an epicentral distance of 70°, the ScS bounce point on the CMB is at an angular distance of ∼34°. Shown are heterogeneity (ULVZ or UHVZ) positions with respect to the ScS bounce point. We discuss waveform behavior in the text based on the ScS bounce point relative to the heterogeneity. In particular, the bounce point is (a) on the near side of the heterogeneity, (b) near the l_1-edge, (c) in the interior of the heterogeneity, (d) near the l_2-edge or (e) on the far-side of the heterogeneity. In each drawing the source is assumed to be at an angular distance of 0° and the receiver at 70°. The blue line shows the ScS ray path traced for PREM. ULVZ definitions are shown in panel (e).

similar to the approach used in Jenkins *et al.* (2021), although the latter study added crucial constraints of which data to use which is discussed later in this paper. This technique works by making a comparison of features in 1-D synthetics to the observations. For these tests, we treat the 2.5-D models as though they were observations. In the previous studies, a catalogue of synthetic waveforms was calculated using either the reflectivity method (e.g. Fuchs & Müller 1971) or the Direct Solution Method (e.g. Cummins *et al.* 1997). In this study, we make computations for 1-D ULVZ models based on the WKBJ method (Chapman & Orcutt 1985). We make a catalogue of 1-D models with δV_S ranging from 0 to −50 per cent in 2 per cent increments, density ($\delta\rho$) fixed at +5 per cent, and thicknesses from 0 to 50 km in 1 km increments. In the WKBJ method the specific ray arrivals must be tabulated. Here we include S, ScS, SdS, ScscS and two additional reverberations within the ULVZ (ScscscS and ScscscscS) in the calculation. For UHVZ models we were unable to match amplitudes of WKBJ synthetics with those calculated with the full waveform method of SHaxi for the larger *S*-wave velocity perturbations. Hence, we computed 1-D UHVZ models also using the SHaxi method. Here we made a catalogue of 1-D models with δV_S ranging from 0 to +30 per cent in 1 per cent increments, density ($\delta\rho$) fixed at +5 per cent and thicknesses from 0 to 40 km in 2 km increments.

We compute FRS traces for the 2.5-D synthetics (treated as data) and the 1-D WKBJ or 1-D SHaxi synthetics. Let us consider the FRS traces for the *i*th 2.5-D SHaxi synthetic model to be $D_i(t)$ representing data, and the FRS traces for the *j*th 1-D WKBJ or 1-D SHaxi synthetic model to be $S_j(t)$ representing the prediction. For each model we calculate the cross-correlation coefficient: $CC(i,j) = D_i(t) * S_j(t)$, where the $*$ denotes cross-correlation. To determine an overall goodness of fit, we modulate the cross-correlation coefficient using two additional weights. The first weight compares the integral of each FRS curve:

$$A(i,j) = 1.0 - \frac{\left|\int_{i=0}^{30} D_i(t)\,dt - \int_{j=0}^{30} S_j(t)\,dt\right|}{\int_{i=0}^{30} D_i(t)\,dt}, \quad (1)$$

where we integrate the FRS traces over the interval from 0 to 30 s. The second weight is based on the maximum or minimum (depending on whether we are testing ULVZs or UHVZs) amplitude of the FRS traces. For example, for the ULVZ models we use

$$M(i,j) = 1.0 - \frac{\left|\max\left(D_i(t)\right) - \max\left(S_j(t)\right)\right|}{\max\left(D_i(t)\right)} \quad (2)$$

In both eqs (1) and (2) the vertical bars (| . . . |) represent the absolute value. Then we consider the best-fitting model to be the model with the maximum value of *G*:

$$G(i,j) = CC(i,j) \times A(i,j) \times M(i,j) \quad (3)$$

3 2.5-D ULVZ ANALYSIS RESULTS

3.1 General characteristics of FRS traces for 2.5-D ULVZ models

2.5-D ULVZ models show more waveform complexity than 1-D models. As an example, in Fig. 4, four-time steps of the wavefield are shown zoomed in on the CMB for a model where the ScS bounce-point is on the far-side of the ULVZ (see Fig. 3e). The first snapshot (Fig. 4a) is shown where the down going *S* wave is interacting with the ULVZ, and we can see the generation of an SdS arrival as well as reverberations within the ULVZ. At 520 s (Fig. 4b) the ScS ray path is just about to bounce off the CMB. We can still see an SdS arrival as a precursor to ScS, but the ScS wavefield looks distorted due to interference with an arrival that looks to be diffracted from the ULVZ boundary. At 570 s (Fig. 4c), the main ScS arrival has overtaken SdS, but a complicated train of coda exists in its wake. At 620 s (Fig. 4d) we see a clearly developed ScS arrival, followed by multiple coda waves. The wavefield shown here is typical of the case when the ScS arrival misses the ULVZ. Even though the ScS bounce point was ∼4° away from the ULVZ, we see that the ULVZ still generates a post-cursory wavefield behind ScS.

Fig. 5 shows example waveforms and FRS processed traces for a ULVZ model with $h = 20$ km, $l = 6°$ and $\delta V_S = -20$ per cent at a variety of positions from $l_1 = 26°$ to $l_1 = 42°$. This model has the most extreme ULVZ properties we tested in this study and is most useful to describe the 2.5-D arrivals as they are more clearly separated in time for this model. The lowermost trace in Fig. 5(a) shows the corresponding 1-D ULVZ model prediction. In the 1-D model we can clearly see the SdS precursor, the ScscS post-cursor and an ScS arrival that is delayed in time due to the ULVZ. We call the latter arrival ScS^U to distinguish it as an arrival that has passed through the ULVZ. The $l_1 = 26°$ trace has a far-side bounce point (Fig. 3e) and shows an ScS arrival that is coincident with the PREM arrival time and so we call it ScS^P. We note that this trace has much more coda

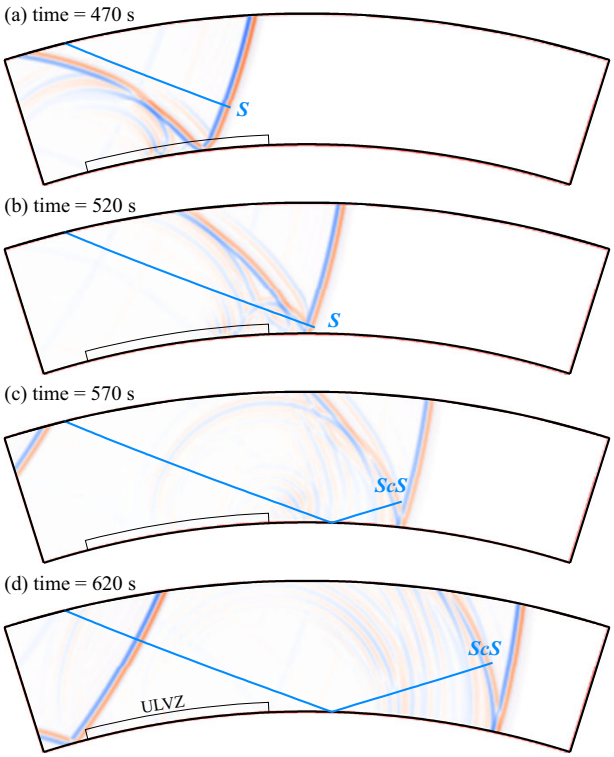

Figure 4. SH-wave velocity wavefield at a time of (a) 470 s, (b) 520 s, (c) 570 s and (d) 620 s for a 500 km deep event with a dominant source period of 5 s. The ULVZ model has $h = 40$ km, $\delta V_S = -20$ per cent, $l_1 = 18^\circ$ and $l = 12^\circ$. The ScS ray path is drawn in blue. Non-linear scaling is applied to wavefield amplitudes to highlight lower amplitude arrivals. An animation of the ray paths and wavefield is given in supplementary online materials Movie_S2.mp4.

energy that the 1-D ULVZ model. The $l_1 = 28^\circ$ and $l_1 = 34^\circ$ traces have bounce points at the l_2 (Fig. 3b) and l_1 (Fig. 3d) edges respectfully. Both of these traces show a multipath ScS arrival with times corresponding to ScS^P and ScS^U. The $l_1 = 30^\circ$ and $l_1 = 32^\circ$ traces have bounce points in the interior of the ULVZ (Fig. 3c) and are the most similar to the 1-D ULVZ model, showing both SdS precursor and ScscS post-cursors. Yet a negative FRS peak exists ahead of the main positive polarity FRS peak due to the persistence of some ScS^P energy in the waveforms. Traces with edges $l_1 \geq 36^\circ$ have near-side ScS bounce points (Fig. 3a). These waveforms also show a complex coda wave train, but the amplitude of these additional post-cursors diminishes as the ULVZ moves to larger l_1-edge positions. All of the 2.5-D predictions show an additional post-cursor arrival.

In Fig. 5(b) the portion of the wavefield that comes before the ScS maximum (blue segments in Fig 5a) are reversed in time and overlain on the portion of the wavefield that comes after the ScS maximum (red segments in Fig. 5a). Hereafter we refer to the reversed time portion of the trace as the reverse trace and the positive time portion of the trace as the forward trace. For the 1-D ULVZ model (lowermost trace in Fig. 5b) we see that the peak of the ScscS and SdS arrivals occur at nearly the same time, but with opposite polarities. When the ScS bounce point is outside of the ULVZ (either a near-side or far-side bounce) we do not see opposite polarity arrivals as clearly, but when the ScS bounce point is on one of the ULVZ boundaries or in the interior of the ULVZ we do see opposite polarity arrivals.

In Fig. 5(c) the FRS traces are shown. The traces in the lowermost row show the FRS trace for 1-D ULVZ model as a solid brown line. This is repeated for all of the 2.5-D FRS traces above it. When the ScS bounce point is at the boundaries or inside the ULVZ, the peak FRS amplitude and timing corresponds well between the 2.5-D FRS traces and the 1-D traces, but there is additional complexity in the 2.5-D FRS traces that does not exist in the 1-D FRS trace.

Jenkins *et al.* (2021) only used data in which visual inspection of the forward and reverse traces showed opposite polarities coincident in time with the FRS peak as a quality control step. This can be quantified by calculating the time domain multiplication between the forward and reverse traces. Where opposite polarities exist, the multiplication trace will be negative. Thus, in what follows we only show the negative side of the multiplication trace and mute the positive amplitudes. As an example, in Fig. 6 we show FRS traces and multiplication traces for the ULVZ model with $h = 10$ km and $\delta V_S = -20$ per cent. This model does not have as extreme of ScS multipathing as the ULVZ model shown in Fig. 5 and is better suited for an introduction of the multiplication traces (we discuss multiplication traces for the other models below). For each l_1 edge position, the peak of the FRS trace is indicated by a red dot. Beneath each FRS trace the multiplication trace is drawn in orange. When the ScS bounce point is within the ULVZ interior ($28^\circ \leq l_1 \leq 34^\circ$) there is an impulsive FRS peak with a corresponding impulsive negative peak in the multiplication trace (indicated with the green dots). For bounce points near the ULVZ boundaries ($l_1 = 26^\circ$ and $l_1 = 36^\circ$), we observe a complicated FRS peak and multiplication trace owing to the presence of ScS multipathing. For bounce points outside of the ULVZ ($l_1 < 26^\circ$ and $l_1 > 34^\circ$), the multiplication trace shows no troughs below a threshold of -0.01. This example illustrates how the multiplication trace could be used to assist in identifying observations where the ScS bounce point is inside or near the ULVZ. For example, one could set a threshold as we have done in Fig. 6, where the magnitude of the multiplication trace must exceed 0.01 and must occur within ± 1 s of the FRS peak. We note that the multiplication trace amplitude of -0.01 is obtained after normalizing the forward and reverse traces to unity. Another possibility is to use the magnitude of the multiplication trace to weigh the observations.

When the ScS bounce point occurs inside the ULVZ the ScS arrival is slowed down. This results in a delay which could be used as an additional criterion to determine whether or not ScS traverses inside the ULVZ. Here we define the delay as:

$$\delta T_{ScS} = T^{obs}_{ScS-S} - T^{ref}_{ScS-S}. \quad (4)$$

Where T^{ref}_{ScS-S} is the PREM ScS-S differential travel, and T^{obs}_{ScS-S} is the observed differential traveltime. However, δT_{ScS} is minimal for the weak ULVZ models. For example, we only expect δT_{ScS} from 0.6 to 0.8 s for the 1-D ULVZ models with $h = 10$ km or $h = 20$ km, respectively, with a *S*-wave velocity reduction of 5 per cent. It is unlikely that such a small δT_{ScS} will be reliably detectable in real data. However for larger velocity reductions (e.g. $\delta V_S = -20$ per cent) we may expect δT_{ScS} from 1.4 to 2.8 s for 10 and 20 km thick ULVZs, respectively. This excess δT_{ScS} may be within resolving limits of real data and should be considered when modelling efforts are suggesting ULVZ models with large *S*-wave velocity contrasts. Synthetic seismograms, forward and reverse traces, and FRS traces, similar to that shown in Fig. 5, are shown for all ULVZ models in the online supplements (Figs S1–S12).

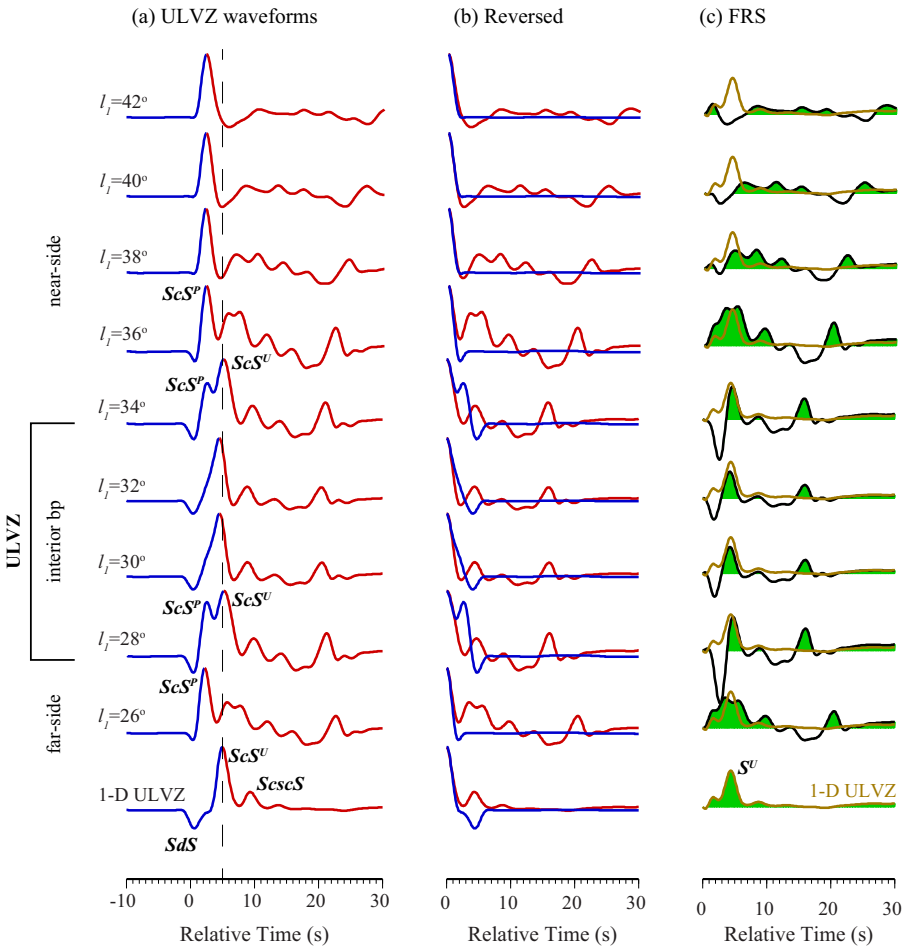

Figure 5. Seismic waveforms and FRS processing for a strong and thick ULVZ model ($\delta V_S = -20$ per cent, $h = 20$ km) with $l = 6°$. (a) ULVZ waveforms are shown aligned in time on the predicted ScS arrival time. The lowermost trace is for the 1-D ULVZ model. All traces above are for 2.5-D ULVZ models with edges as indicated from $l_1 = 26°$ to $l_1 = 42°$. Waveforms are separated into the portion that occurs before the ScS maximum (blue) and the portion that occurs after the ScS maximum (red). (b) The portion of the waveform (blue) that occurs before the ScS maximum is reversed in time and overlain on the waveform portion that occurs after the ScS maximum (red). (c) The lowermost trace, in this panel, with solid brown line and green fill is the FRS trace for the 1-D ULVZ model. For reference the solid brown line is repeated for all traces above. The 2.5-D FRS traces are shown for each edge position with solid black lines and green fill.

3.2 Using 1-D methods to infer ULVZ characteristics for 2.5-D ULVZ models

In this section we consider the 2.5-D synthetics as real observations and we determined the best-fitting ULVZ model based on the fitting method of Zhao *et al.* (2017) as described in Section 2. We will first discuss the results for the strong and thick ULVZ model as this model shows the clearest signals and provides a baseline for which we can discuss the other cases.

3.2.1 Thick/strong ULVZ model ($h = 20$ km, $\delta V_S = -20$ per cent)

Results for all three ULVZ lengths (l) are shown for a thick and strong ULVZ model in Fig. 7. In this figure we show the best-fitting thickness (h) and S-wave velocity contrast (δV_S) as a function of l_1-edge position of the 2.5-D ULVZ. For comparison, we draw in the true values with dashed blue lines. Each datum is shaded by δT_{ScS} as defined in eq. (4). Here we measured ScS-S in the 2.5-D synthetics for T^{obs}_{ScS-S}. Hence, we expect a positive δT_{ScS} (reddish colour) when ScS passes through the ULVZ. We also calculated the multiplication trace and required the amplitude of the multiplication trace to be lower than a threshold of -0.01 occurring within ± 1 s of the FRS peak as an indicator of opposite polarity arrivals. The threshold value was chosen by trial-and-error in an attempt to capture negative polarity arrivals that were visually apparent. If opposite polarities exist, we use a circle symbol, otherwise we use a square. An example of how well the method works for a single ULVZ model is shown in the online supplements (Fig. S13).

In all cases shown in Fig. 7, we observe a positive δT_{ScS} when the ScS bounce points are interior to the ULVZ. In the corresponding 1-D ULVZ model a δT_{ScS} of up to 2.8 s is predicted. This large δT_{ScS} is not observed for the smallest scale ULVZ model [$l = 3°$ in panels (a) and (d)]. But larger δT_{ScS} values are accrued as the ULVZ length is increased. For a length of 12°, ULVZ locations where the ScS bounce point is inside the ULVZ show δT_{ScS} from 2.5 to 3.0 s and are most similar to the 1-D model prediction. When the ScS bounce point is outside of the ULVZ we see a sharp decrease in δT_{ScS} values to near zero. That is, we see little difference between

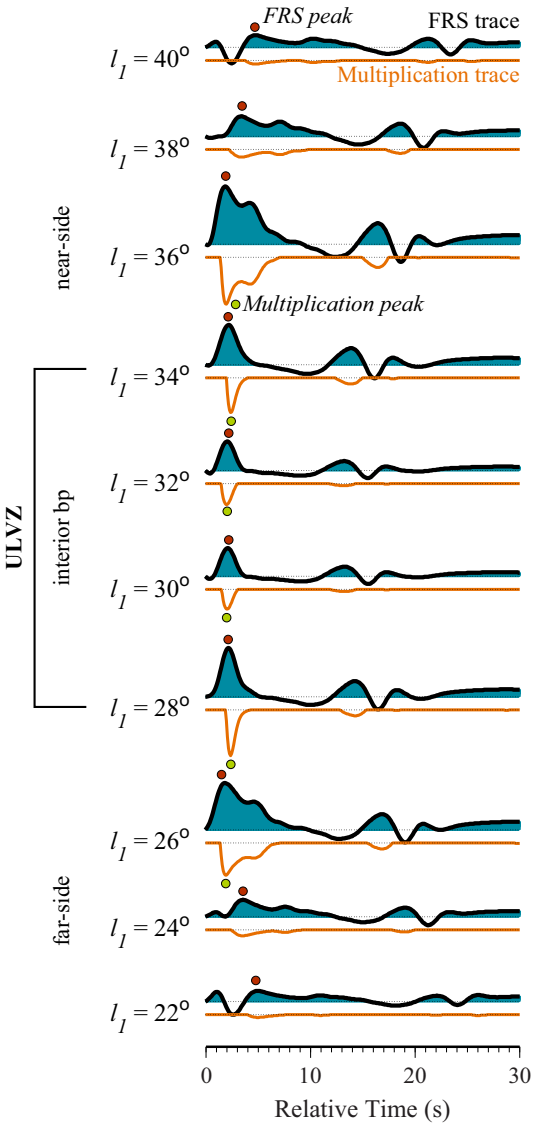

Figure 6. FRS traces and time domain multiplication traces for a 2.5-D ULVZ model with $l = 6°$, $h = 10$ km and $\delta V_S = -20$ per cent. The FRS trace is shown (black trace with blue fill) for l_1 edge positions from 22° to 40°. The peak of the FRS trace is indicated by the red dots. The multiplication trace is shown in orange immediately beneath the FRS trace. If the multiplication trace had a negative peak below −0.01 within ±1 s of the FRS peak it is flagged as a potential ULVZ arrival and marked here with a green circle.

the ScS-S differential traveltimes and those predicted by PREM. Thus, if measurable, a positive δT_{ScS} could be a strong indicator of ULVZ presence.

When the ScS bounce points are inside the ULVZ the multiplication trace always detects opposite polarity arrivals in the forward and reverse traces (circle symbols in Fig. 7). However, opposite polarities are also detected for ScS reflections outside the ULVZ, for up to 8° away from the ULVZ boundary (see e.g. Fig. 7d). Thus, detection of opposite polarities in the forward and reverse traces may not alone be able to constrain ULVZ presence.

As shown in Fig. S13, there are trade-offs in modelling the FRS trace between ULVZ thickness and *S*-wave velocity decrease. This is manifest in the recovered models shown in Fig. 7. For example, in Fig. 7(d), at an edge position of $l_1 = 31°$, the ScS bounce point is within a 20-km-thick ULVZ, but the recovered model shows a ULVZ thickness of 7 km. Because of the trade-offs, this results in an overestimation of *S*-wave velocity (Fig. 7a), which is −29 per cent (true model has $\delta V_S = -20$ per cent). The difference in waveforms between the recovered model and true model are negligible and thus one must be aware that large uncertainties exist in inferring ULVZ parameters from this approach.

When the ScS bounce points are outside of the ULVZ we also get FRS peaks in the 2.5-D ULVZ models. This is in large part due to the additional post-cursory energy that exists for 2.5-D morphologies. As can be seen in all panels of Fig. 7, 1-D modelling of these FRS peaks may also result in ULVZ detections, some of which have large modelled thicknesses and ULVZ velocity decreases. These would result in spurious detections but would not be considered if it is possible to detect both a positive δT_{ScS} and opposite polarity arrivals.

Jenkins *et al.* (2021) also used a traveltime mask to ensure that only models with realistic traveltime delays were accepted. We tried using such a mask in these tests. The traveltime masks helped to reduce the large thickness and velocity contrasts that is sometimes recovered for ScS bounce points outside of the ULVZ. This is because in these cases the extra post-cursory energy sometimes generates FRS peaks at larger times than what is measured. Thus, those solutions can be ignored. However, for ScS bounce points inside the ULVZ the FRS peak was due to the ULVZ and always gave a delay time that was less than or equal to the 1-D prediction. Nevertheless, using a traveltime mask can also reduce spurious ULVZ detections.

3.2.2 *Thin/strong ULVZ model ($h = 10$ km, $\delta V_S = -20$ per cent)*

Results for the thin/strong ULVZ model are shown in Fig. S14. In almost all respects, the results for these models are similar to those described in the previous sub-section (3.2.1). The most notable difference is that we find opposite polarity arrival detections within about 4° of the ULVZ, as opposed to 8° in the previous case. That is, the detection of opposite polarities in this case provides better constraints on ULVZ position.

3.2.3 *Thick/weak ULVZ model ($h = 20$ km, $\delta V_S = -5$ per cent)*

Results for the thick/weak ULVZ models are shown in Fig. S15. In this case we find good agreement between recovered model parameters and true ULVZ parameters for the largest scale ULVZ ($l = 12°$, Figs S15c and f). Observations are generally consistent with what has been discussed in the previous two subsections. But, for smaller length ULVZs ($l = 6°$ and $l = 3°$) we no longer detect opposite polarity arrivals for ScS bounce points in the centre of the ULVZs. Here the ScscS post-cursor has a low amplitude, and the peak of the multiplication trace drops below the threshold we set. However, near the ULVZ boundaries (e.g. at $l_1 = 28°$ and $l_1 = 34°$ in Figs S15b and e) we do observe negative polarity arrivals. Here the ScscS post-cursor amplitude is increased by the presence of a low amplitude ScS^U multipath arrival. For these models, δT_{ScS} values are small with a maximum of 0.8 s predicted in the PREM model. Again, this large of δT_{ScS} is observed in the large 12° length models but is lower in the smaller length models. It may be challenging to measure such a small δT_{ScS} value in real data.

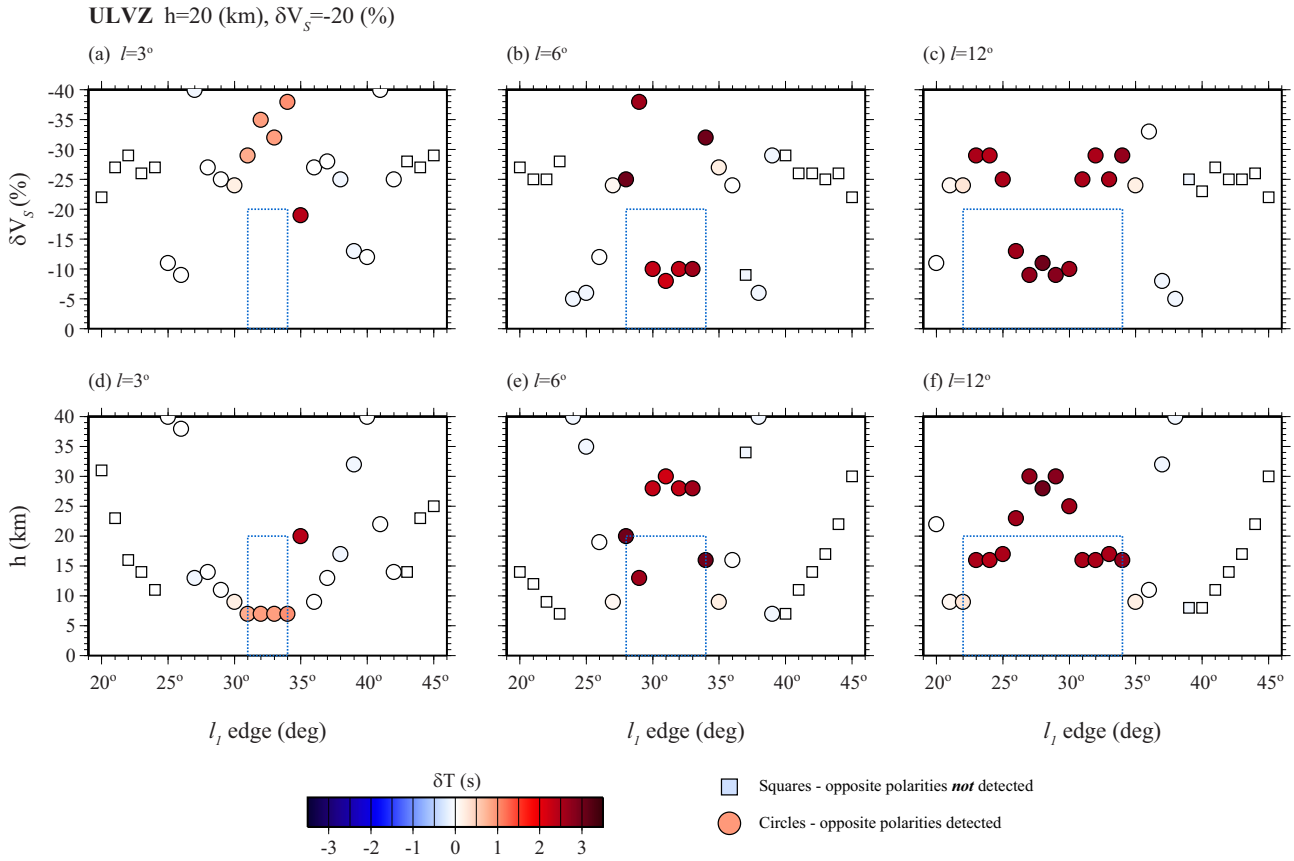

Figure 7. Testing the waveform fitting method of Zhao *et al.* (2017) against 2.5-D synthetic predictions. This figure shows the results for a ULVZ model with $h = 20$ km and $\delta V_S = -20$ per cent. Results for ULVZ lengths of $l = 3^\circ$ are shown as (a) δV_S and (d) thickness. ULVZ lengths of $l = 6^\circ$ are shown as (b) δV_S and (e) thickness. UHVZ lengths of $l = 12^\circ$ are shown as (c) δV_S and (f) thickness. In each panel, symbols indicate the recovered parameter and are shaded by δT_{ScS} (see text for definition). Symbols are circles or squares depending on whether positive/negative pair arrivals are detected in the forward and reverse traces. The true model values are shown with dashed blue lines.

3.2.4 Thin/weak ULVZ model ($h = 10$ km, $\delta V_S = -5$ per cent)

Results for the thin/weak ULVZ models are shown in Fig. S16. Again for the largest length ULVZ models ($l = 12^\circ$, Figs S16c and f), the ULVZ parameters are well recovered and the multiplication trace does a good job of detecting opposite polarity arrivals for ScS bounce points within the ULVZ. δT_{ScS} values are small. But, for the small scale ULVZs ($l = 6^\circ$ and $l = 3^\circ$), we do not detect opposite polarity arrivals within the ULVZ. These thin/weak ULVZs of small lateral dimensions show FRS peaks that can be modelled by the fitting technique, but confirmation of ULVZ presence may be difficult.

3.3 Summary of 2.5-D ULVZ modelling results

To summarize,

1) When the ScS bounce point is within the ULVZ we expect to observe a positive δT_{ScS} value. For ULVZ models with larger *S*-wave velocity reductions, this excess δT_{ScS} may be several seconds. But for weaker ULVZ models δT_{ScS} may only be a few tenths of seconds and not be measurable.

2) At the time of the FRS peak, there are positive and negative polarity arrivals evident in the forward and reverse traces, respectively. This can be quantified by calculating the time domain multiplication between the forward and reverse traces (prior to flipping the reverse trace). For the boxcar ULVZ models tested here, the opposite polarities are not always confined to the ULVZ interiors but may extend up to several degrees away from the ULVZ boundaries. Thus, the opposite polarities alone are not enough to constrain ULVZ boundaries but can provide approximate boundaries. For the weak ULVZ heterogeneity (−5 per cent) of smaller lateral scales (3° to 6°) the opposite polarity detections were below our cut-off thresholds and would be difficult to confirm in real data.

3) There is a strong trade-off between h and δV_S. Analysis of trade-off curves (e.g. Fig. S13) shows that the trade-off is more widely distributed in δV_S than in h. As a result, ULVZ thickness may be better constrained.

4) A positive FRS peak almost always exists in the 2.5-D synthetics. Thus, proper interpretation of FRS traces in data requires some caution. As suggested in the above points, a first step should be to discard observations where clear positive and negative arrivals are not observed in the forward and reverse traces. A second step could be to determine if excess δT_{ScS} exists.

5) The predicted δT_{ScS} for 1-D models is only observed here for the ULVZ models with the largest lateral size ($l = 12^\circ$). The measured δT_{ScS} for the smallest models ($l = 3^\circ$) may only be on the order of half of that for the 1-D models.

4 UHVZ ANALYSIS

In this section we provide a similar analysis for UHVZ models. However, the nature of the arrivals in UHVZs is more complicated

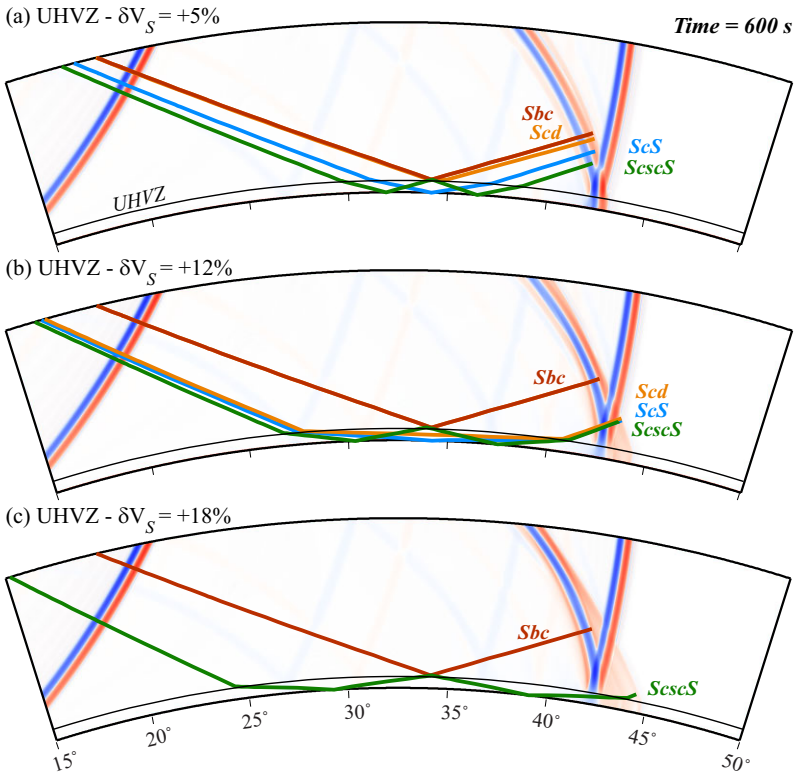

Figure 8. Three snapshots of the SH-velocity wavefield and ray paths at time 600 s for three different 40-km-thick UHVZ models: (a) $\delta V_S = +5$ per cent, (b) $\delta V_S = +12$ per cent and (c) $\delta V_S = +18$ per cent. Show ray paths and wavefield. Non-linear scaling is applied to wavefield amplitudes to highlight lower amplitude arrivals. Calculations are for a 500 km deep source. Animations for the wavefield and ray paths for the three examples above are provided in the online supplements as Movie_S3, Movie_S4 and Movie_S5.

than that for ULVZ models. So, we begin with a general discussion of the arrivals present in 1-D UHVZ models.

4.1 1-D UHVZ models

UHVZ models possess a unique challenge in interpreting arrivals that are not encountered when considering ULVZ models. Namely, the number of arrivals present for 1-D UHVZ models varies depending on the UHVZ thickness and velocity contrast. In addition, the relative polarity and phase shift of these arrivals varies significantly across the range of UHVZ models considered in this paper, which is not the case for ULVZ structures. Fig. S17 in the online supplements shows predicted traveltimes for 1-D UHVZ models based on ray tracing with the TauP Toolkit (Crotwell *et al.* 1999). SHaxi synthetic predictions for 1-D UHVZ models are shown in Fig. S18 overlain on the TauP predictions. These two figures are presented for reference in the supplements as aids in deciphering what arrivals one may expect for UHVZ models. But we must emphasize that these figures are made at only one distance (70°) and one event depth (500 km). UHVZ arrivals depend on the angle of incidence of the downgoing *S* wave, the velocity contrast of the UHVZ, the thickness of the UHVZ, and are thus also dependent on event depth and source–receiver distance. Nonetheless, since we will document changes for different UHVZ structure properties, we hold source depth and distance constant (as we did for ULVZ structures).

For UHVZ heterogeneities with mild velocity increases (i.e. $\delta V_S = +8$ to $+15$ per cent for 5–40-km-thick UHVZs), we observe SdS arrivals similar to those encountered for a velocity increase with the D'' discontinuity. In this case we have a reflected Sbc arrival and a refracted Scd arrival, which we collectively refer to as SdS (e.g. Whittaker *et al.* 2016). In addition, we observe ScS and ScscS arrivals. For the smallest velocity increases, the Sbc arrival is precursory to ScS whereas the ScscS arrival is a post-cursor. For UHVZ thickness $\leq$20 km (Figs S17 and S18) these arrivals are closely spaced in time causing a slight broadening of what appears to be a single ScS pulse. For a 40-km-thick UHVZ (Fig. S18) we are able to distinguish between individual arrivals. Ray paths and wavefield for a 1-D UHVZ model with $h = 40$ km and a low velocity contrast of $\delta V_S = +5$ per cent are shown in Fig. 8(a).

Increasing the velocity contrast to +12 per cent (Fig. 8b) still shows all 4 arrivals for a 40-km-thick UHVZ. However, increasing the velocity contrast ultimately reduces the number of arrivals that are present. This is because some of the arrivals that pass into the UHVZ in previous cases become post-critical. In this case, SdS consists solely of a post-critical Sbc reflection. For example, in Fig. 8(c), we show a 1-D UHVZ model with $h = 40$ km and $\delta V_S = +18$ per cent. Here we have the Sbc reflection and ScscS arrivals, but no Scd or ScS arrivals. At the largest velocity contrasts, we have just two arrivals. The first arrival is an emergent ScscS arrival. The second arrival is a phase shifted Sbc reflection. These arrivals are all labelled in Fig. 2(d). The complex waveform shape shown at the bottom of Figs 2(d) and (e) ($h = 20$ km and $\delta V_S = +20$ per cent) shows a reverse trace (blue portion) that consists of both the ScscS precursor and the positive polarity portion of the Sbc precursor. But the forward trace (red portion) consists of the negative polarity portion of the phase shifted Sbc precursor. But for a different UHVZ

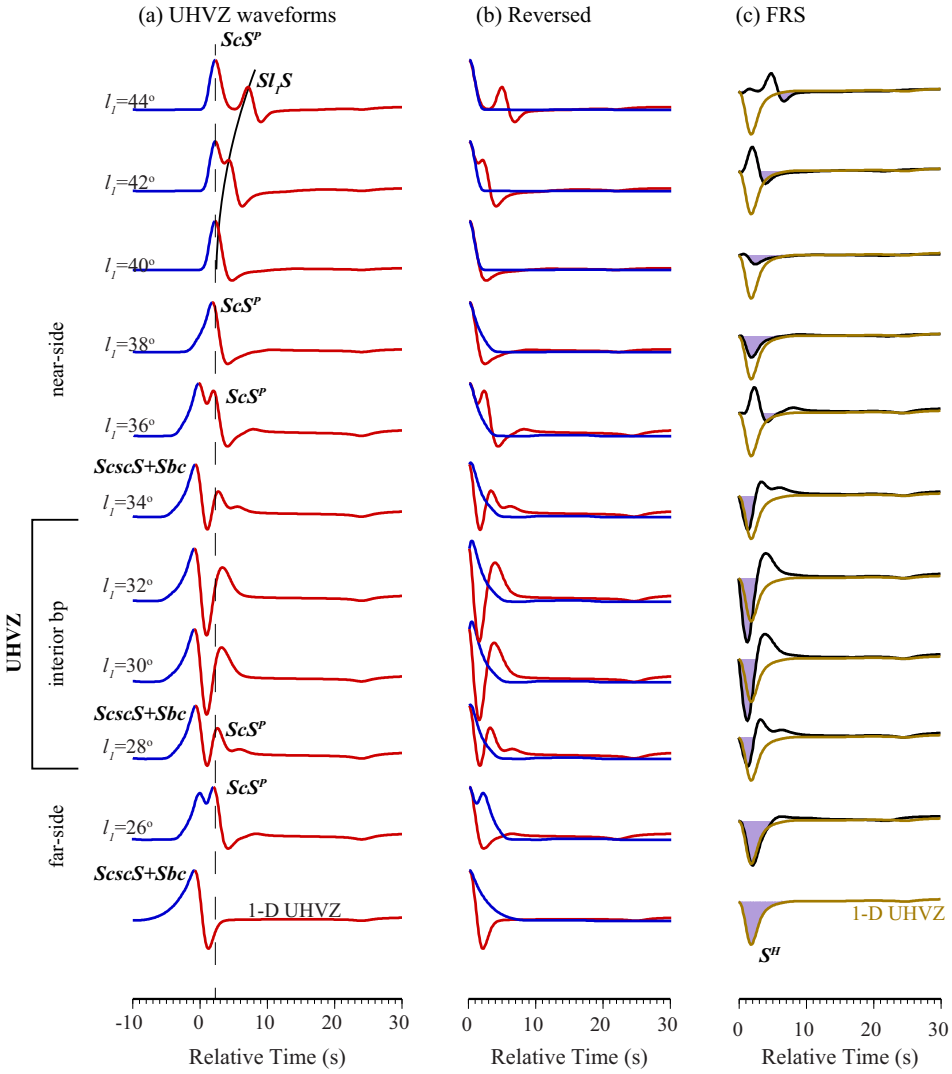

Figure 9. Seismic waveforms and FRS processing for a strong and thick UHVZ model ($\delta V_S = +20$ per cent, $h = 20$ km) with $l = 6^\circ$. (a) UHVZ waveforms are shown aligned in time on the predicted ScS arrival time for PREM. The lowermost trace is for the 1-D UHVZ model. All traces above are for 2.5-D UHVZ models with edges as indicated from $l_1 = 26^\circ$ to $l_1 = 44^\circ$. Waveforms are separated into the portion that occurs before the ScS maximum (blue) and the portion that occurs after the ScS maximum (red). (b) The portion of the waveform (blue) that occurs before the ScS maximum is reversed in time and overlain on the waveform portion that occurs after the ScS maximum (red). (c) The lowermost trace with solid brown line and green fill is the FRS trace for the 1-D UHVZ model. For reference the solid brown line is repeated for all traces above. The 2.5-D FRS traces are shown for each edge position with solid black lines and green fill.

model such as shown in the 2nd trace down from the top of Figs 2(d) and (e) ($h = 10$ km and $\delta V_S = +20$ per cent), the reverse trace (blue portion) consists of all three arrivals ScS, positive portion of Sbc and ScscS. Whereas the forward trace (red trace) just shows a low amplitude negative polarity peak that is the negative portion of the phase shifted Sbc arrival. Despite these complexities in arrivals, the 1-D UHVZ models show a negative FRS trace (called S^H in Fig. 2f) except for the thin/weak UHVZ model ($h = 10$ km and $\delta V_S = +10$ per cent) as shown in Figs 2(d) and (f). We note that this discussion is specific to the epicentral distance of 70°. There are variations at other distances, especially with respect to the phase shift of the Sbc arrival. For reference, full waveform synthetics for 620 different 1-D UHVZ models are included for distances from 55° to 95° in the online data.

For the 1-D UHVZ models shown in Fig. 8, the ScscS ray path extends across larger angular distances with increasing *S*-wave velocity. In Fig. 8(a) we can see that the ScscS ray path is contained within the UHVZ for an angular distance less than approximately 10° (~600 km) for a 5 per cent velocity increase. But, for a 18 per cent velocity increase (Fig. 8c) a laterally continuous UHVZ of nearly 20° length (~1300 km) in the great circle arc direction is required. Thus, if UHVZs exist with smaller lateral dimensions the ScscS arrival will not exist as shown in 1-D models.

4.2 2.5-D UHVZ models

Predictions for a 1-D and 2.5-D UHVZ model are shown in Fig. 9. In 1-D (bottom row in Fig. 9a) only Sbc and ScscS arrivals are predicted. But in this figure, we show UHVZ models with a length of $l = 6^\circ$ which is too small (~380 km) to contain the lateral extent of a ScscS arrival (see Fig. 8). This results in a complex UHVZ

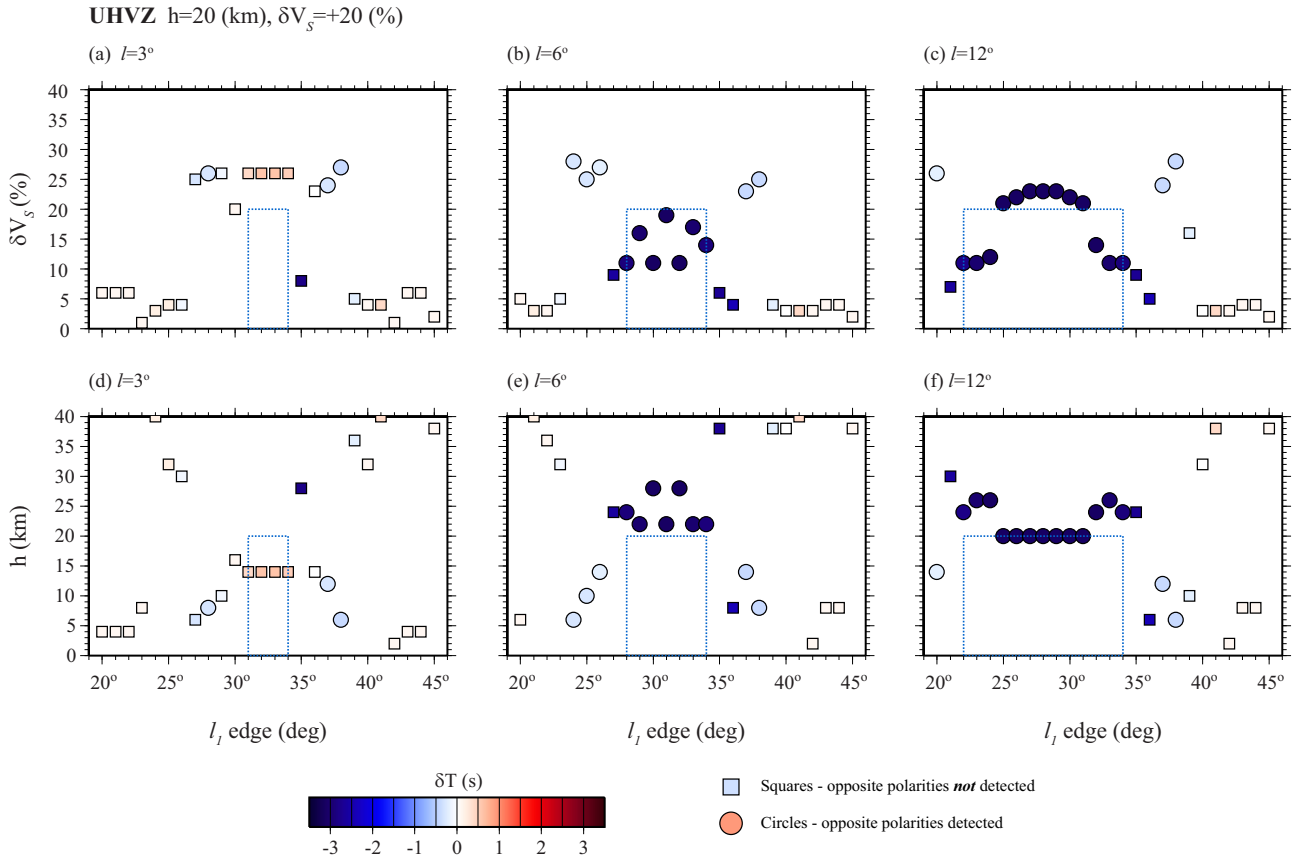

Figure 10. Testing the waveform fitting method of Zhao *et al.* (2017) against 2.5-D synthetic predictions. This figure shows the results for a UHVZ model with $h = 20$ km and $\delta V_S = +20$ per cent. Results for UHVZ lengths of $l = 3^\circ$ are shown as (a) δV_S and (d) thickness. UHVZ lengths of $l = 6^\circ$ are shown as (b) δV_S and (e) thickness. UHVZ lengths of $l = 12^\circ$ are shown as (c) δV_S and (f) thickness. In each panel, symbols indicate the recovered parameter and are shaded by δT_{ScS} (see text for definition). Symbols are circles or squares depending on whether positive/negative pair arrivals are detected in the forward and reverse traces. The true model values are shown with dashed blue lines.

waveform for the finite length UHVZ models. For large edge positions ($l_1 \geq 42^\circ$ in Fig. 9a) an additional post-cursor exists that we refer to as Sl_1S. This post-cursor exists for near-side bounces (Fig. 3a) and is an edge diffraction off of the near-side of the UHVZ. Sensitivity tests (shown in supplemental Fig. S19) demonstrate that the timing of this arrival is primarily dependent on UHVZ l_1-edge location. That is, the farther away the UHVZ is from the ScS bounce point the later in time this arrival occurs. It is slightly dependent in time on UHVZ thickness with thicker UHVZs generating earlier arrivals. There is no dependence on *S*-wave velocity for arrival times, however the *S*-wave velocity does control the amplitude of this arrival. As seen in Fig. 9(c), this extra post-cursor does create a negative FRS peak. However, we observe no peak in the multiplication trace as no opposite polarity arrival is coincident in the reverse trace, and so long as the multiplication traces are consulted, this arrival should not be confused as useful signal in the FRS traces.

When the ScS bounce point is outside of the UHVZ we can observe an ScS arrival at the PREM predicted arrival time (see Fig. 9a, $l_1 = 26^\circ$ or $l_1 = 44^\circ$ labelled ScS^P). But, inside the UHVZ the ScS arrival is predicted to disappear in this UHVZ model. However, some ScS energy appears to persist for the edge-located bounce points and possibly for some the interior bounce points. For all UHVZ locations near the boundary or within the UHVZ a Sbc precursor exists with the largest amplitude. This Sbc arrival dominates the waveform for this UHVZ model, with only a low amplitude ScscS precursor ahead of it. The Sbc post-cursor wavefield is complicated and appears to be complicated by diffracted arrivals from the boundaries of the UHVZ. A parameter sensitivity test for the $l_1 = 30^\circ$ position is given in Fig. S20. 2.5-D waveform predictions, forward and reverse traces, and FRS traces for all UHVZ models are shown in the online supplements (Figs. S21-S32).

4.3 Using 1-D methods to infer UHVZ characteristics for 2.5-D UHVZ models

4.3.1 Thick/strong UHVZ model ($h = 20$ km, $\delta V_S = +20$ per cent)

Recovered models using the fitting approach of Zhao *et al.* (2017) for a thick and strong UHVZ model are shown in Fig. 10. At the largest length scales ($l = 6^\circ$ and 12°, Figs 10b, e and c, f) the 1-D modelling approach does a good job to fit the UHVZ model for the interior bounce points. A δT_{ScS} advance of -3.0 s is predicted in the 1-D UHVZ model and is realized for the large length scale model. We must use caution in our interpretation here, as what is actually being measured in both the 1-D and 2.5-D UHVZ models is the differential traveltime between *S* and the Sbc reflection from the top of the UHVZ, as no ScS arrival is predicted to exist for the interior bounce points. The δT_{ScS} advance plummets to near zero within 2° of the UHVZ boundaries and could be diagnostic of UHVZ presence.

For these longer lateral dimension UHVZ models, the multiplication trace also shows good diagnostic capabilities for detecting the UHVZ boundaries. We observe that opposite polarities are detected for the interior bounce points (e.g. dark blue circles in Figs 10b, e and c, f). Here the opposite polarities being detected are the positive and negative portions of the phase shifted Sbc arrival reflecting off the top of the UHVZ. However, some opposite polarity arrivals are detected for exterior bounce points. For example, notice the light blue circle at $l_1 = 38^\circ$, in Fig. 10(f). An additional negative polarity post-cursor (see Fig. S32, l_1 from 38° to 44°) is causing interference in this case that is giving rise to this opposite polarity observation. Thus, one must use caution, as the complex ScS post-cursory wavefield generated by the finite length UHVZs may culminate in spurious opposite polarity observations. Strong trade-offs between *S*-wave velocity contrast and thickness also exist in the UHVZ models. This is notably demonstrated in Figs 10(b) and (e). For the interior bounce points we see that in general if the UHVZ thickness is overestimated that is compensated for by a smaller velocity contrast.

For the smallest UHVZ lengths ($l = 3^\circ$), shown in Figs 10(a) and (d), the FRS method fails. For this small UHVZ lateral length, the waveforms are dominated by a combination of the Sbc arrival and a later arriving ScS^P wave initiating in normal mantle outside of the UHVZ (see Fig. S30). Here the ScS arrival has the larger amplitude. This results in a strongly negative S^H FRS trace that is coincident in time with the later arriving ScS^P arrival and not the Sbc arrival. In addition, instead of observing a δT_{ScS} advance, we observe a slight delay, and we do not observe opposite polarity detections for the interior bounce points.

4.3.2 Thin/strong UHVZ model (h = 10 km, $\delta V_S = +20$ per cent)

Results for the thin/strong UHVZ models are shown in Fig. S33 and mimic the general results for the thick/strong UHVZ discussed in the previous subsection (4.2.2).

4.3.3 Thick/weak UHVZ model (h = 20 km, $\delta V_S = +10$ per cent)

Results for the thick/weak UHVZ model are shown in Fig S34. Again, these results largely mimic those described above, except for one major distinction. For these weak velocity heterogeneities there is almost no detectable opposite polarity arrivals. As a result, we see in all panels of Fig. S34 that we did not detect a single opposite polarity arrival. Nevertheless, a detectable negative S^H FRS trace is observed (see e.g. Fig. S26) that can be modelled for the larger UHVZ lengths ($l = 6^\circ$ and $l = 12^\circ$ as shown in Figs S34(b), (e) and (c), (f). However, the amplitude of the multiplication trace is below the detection threshold that we set for all of these models.

4.3.4 Thin/weak UHVZ model (h = 10 km, $\delta V_S = +10$ per cent)

The results for the thin/weak UHVZ model are shown in Fig. S35. These results mimic those of the previous subsection for the thick/weak UHVZ model (in Section 4.2.3).

4.4 Summary of 2.5-D UHVZ modelling results

To summarize,

1) When the ScS bounce point is within the UHVZ we expect to observe a δT_{ScS} advance. For UHVZ models with larger *S*-wave velocity increases, this advance may be several seconds. But for weaker UHVZ models the delay may only be a few tenth of seconds and not be measurable. For the larger *S*-wave velocity increases we are not actually measuring the differential traveltimes between S and ScS, but between *S* and the UHVZ reflected Sbc arrival.

2) At the time of the negative FRS peak for UHVZ models (S^H), there are positive and negative polarity arrivals evident in the forward and reverse traces respectively for the large length models ($l = 6^\circ$ and $l = 12^\circ$) but not for the small length models ($l = 3^\circ$). This can be quantified by calculating the time domain multiplication between the forward and reverse traces. For the boxcar UHVZ models tested here, the opposite polarities are not always confined to the UHVZ interiors but may extend up to several degrees away from the UHVZ boundaries. Thus, the opposite polarities alone are not enough to constrain UHVZ boundaries but can provide approximate boundaries.

3) Large trade-offs exist between h and δV_S. As a result, UHVZ parameters recovered with this method are highly uncertain.

4) A negative FRS peak almost always exists in the 2.5-D synthetics. Thus, proper interpretation of FRS traces in data requires some caution. As suggested in the above points, a first step should be to discard observations where clear positive and negative arrivals are not observed in the forward and reverse traces. A second step could be to determine if excess traveltime delays exist. However, for the weak UHVZ heterogeneities (+10 per cent) we see a well-defined FRS peak (S^H) that shows virtually undetectable negative polarity arrivals in the multiplication traces, and only small δT_{ScS} advances.

5 APPLICATION TO DATA

Zhao *et al.* (2017) applied the FRS technique to data sampling the Eastern Pacific Ocean region along the northeastern boundary of the Pacific LLVP inferring the existence of ULVZs in the region. Multiple additional studies have demonstrated overlapping ULVZ presence (Lay *et al.* 2006; Liu *et al.* 2011; Sun *et al.* 2019; Jenkins *et al.* 2021; Lai *et al.* 2022; Wolf & Long 2023). Of the events examined in Zhao *et al.* (2017), we selected the $M_w = 6.4$, 233 km deep event of 22 October 2008 (12:55) to use as a case study to test how well the observations we made in the previous sections can be utilized. We obtained the source depth and focal mechanism for this event from the United States Geological Survey (USGS) National Earthquake Information Center (NEIC) catalogue. For this event we collected data available in North America from the Incorporated Research Institutions for Seismology (IRIS) and the Southern California Earthquake Center (SCEC). For each record in this event we, (1) removed the instrument response, (2) rotated to transverse component and (3) individually examined each trace removing traces where both S and ScS could not be unambiguously identified. We included data in the epicentral distance range from 60° to 90° and in the azimuthal band from 30° to 56° for further analysis. Even though we allowed for data in the range from 60° to 90°, only data from roughly 74° to 90° actually existed for this event in these azimuths. After quality control steps we retained 834 seismic traces of the 1088 records in the cited azimuth and distance bounds. All data were bandpass filtered with corners between 1 and 100 s.

The event and station locations are shown in Fig. 11(a), with ScS bounce points on the CMB indicated with circles. Fig. 11(b) shows these locations in reference to *S*-wave tomography model S40RTS at the CMB (Ritsema *et al.* 2011). The average great circle path

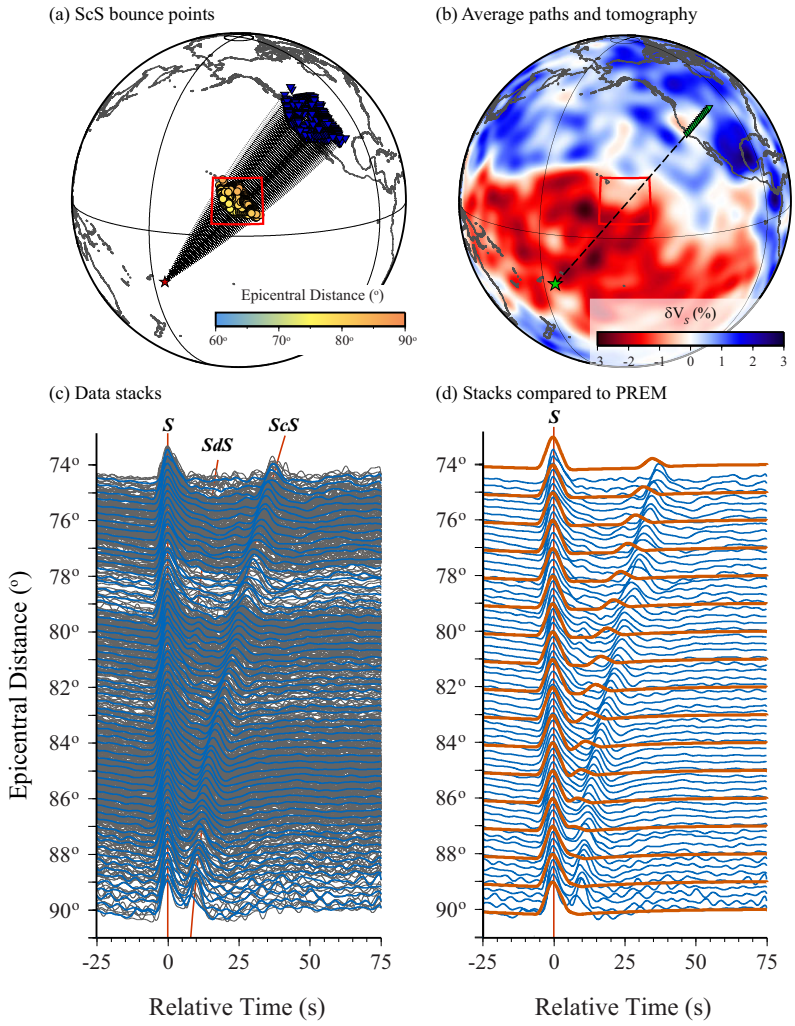

Figure 11. Distance profile and location map for 22 October 2008 (12:55) event. (a) Map showing the event location (red star) and receiver locations (inverted blue triangles). The ScS bounce points on the CMB are drawn with circles shaded by the source–receiver epicentral distance. The red box outlines the area between latitudes of 5° to 21° and longitudes from −158° to −140°. (b) The event (green star) and virtual receivers (green triangles) at distances from 74° to 86° are shown along the average azimuth of 43°. The black dashed line shows the great circle path along this average azimuth. The background shows *S*-wave velocity from tomography model S40RTS (Ritsema *et al.* 2011). (c) Distance profile for the event. Data are aligned on the peak of the direct *S*-wave arrival. Individual traces are shown in gray and are stacked into 0.25° epicentral distance bands shown in blue. (d) Stacks (blue) are shown overlain on PREM predicted synthetic seismograms (orange). All records are transverse component displacement traces.

is shown by the dashed black line which is used for modelling as described below. Here we can see that the ScS bounce points are located near the boundary of the Pacific LLVP. A distance profile showing original traces (grey) and stacks (blue) in 0.25° distance increments are shown in Fig. 11(c). These stacks are overlain on synthetics computed for the PREM model (orange traces) in Fig. 11(d). Interesting features can be seen in the raw waveforms. Most notable is that in these data the ScS arrival persists as a separable arrival all of the way to an epicentral distance of 90°, whereas in the PREM waveforms (orange traces in Fig. 11d) ScS and the direct *S* wave have merged by roughly 87°. At all distances, ScS is delayed with respect to the PREM prediction. Furthermore, a noticeable SdS arrival from the *D″* discontinuity can be seen and is especially prominent at distances between 79° and 81°. Another positive amplitude precursor is observable ahead of the ScS arrival at distances between 75° and 77°.

We sort records into geographical bins based on ScS bounce point on the CMB. We use a 1° radius bin and require a minimum of 15 records in each bin. For each geographical bin we compute the FRS stack and the multiplication trace. In contrast to all previous FRS studies, we do not conduct a source deconvolution. Rather we construct an empirical source–time function by first stacking direct *S*-wave arrivals in the distance range from 74° to 84°. We then convolve a Gaussian wavelet with a triangle function to best match the stacked *S*-wave arrivals. This empirical source can be convolved with the synthetic Green's functions to mimic the duration and shape of the original arrivals (see e.g. Thorne & Garnero 2004). In addition, we measure δT_{ScS} where an ScS arrival is present in both observations and PREM predictions.

Results for this event are shown in Fig. 12. In Fig. 12(a) we summarize the results from the FRS traces as a function of geographic bin. The time to the peak of the FRS trace is indicated by

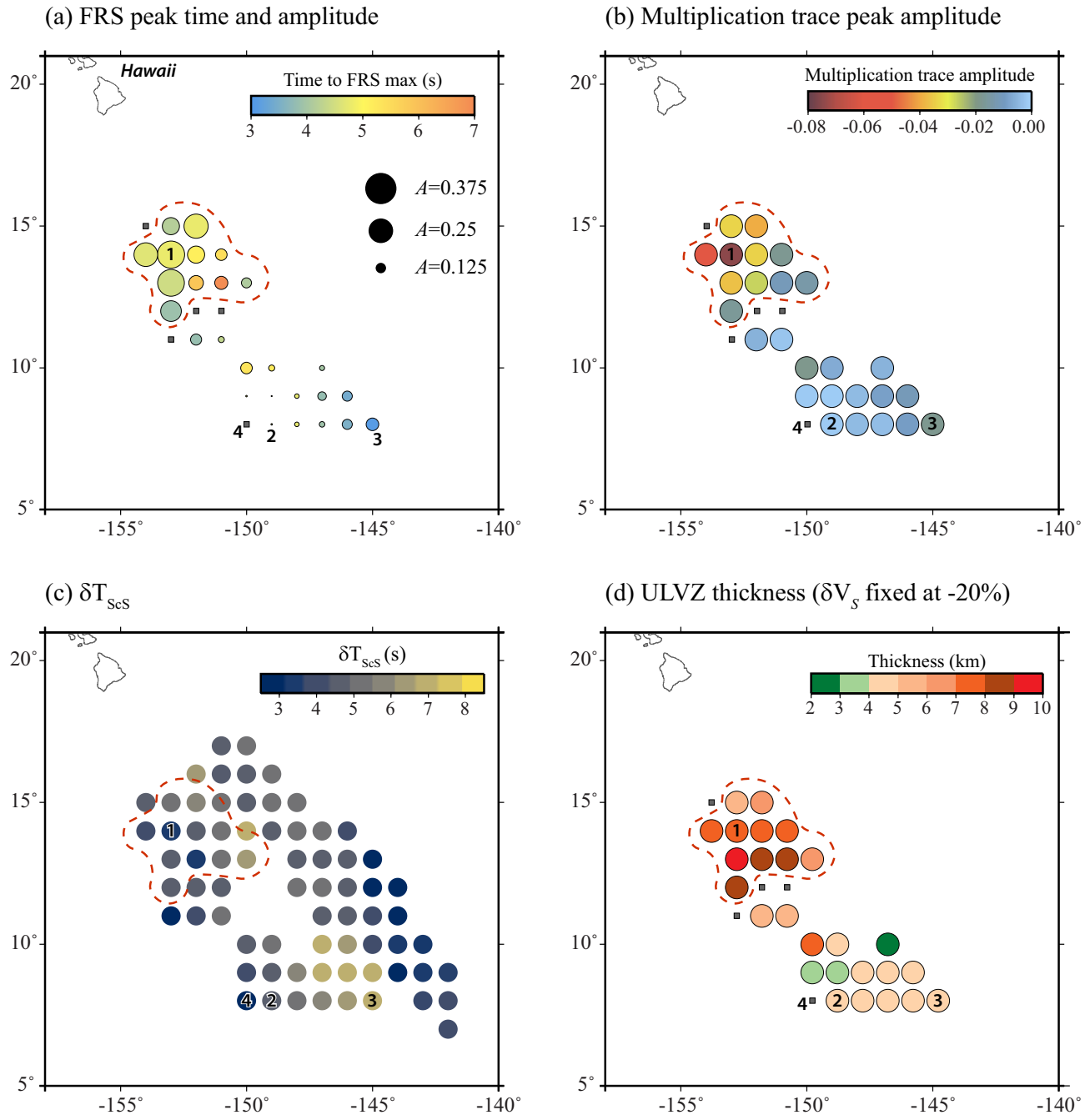

Figure 12. (a) Each circle represents a geographic bin location for which we calculated an FRS trace for which a negative peak was found in the multiplication trace within ±1 s of the FRS peak time. The circles are shaded by the time of the FRS peak and are scaled in size by the amplitude of the FRS peak relative to the ScS amplitude. Gray squares indicate that no peak was found in the multiplication trace. (b) For each circle shown in the previous panel, we shade the circle in this panel by the amplitude of multiplication trace minimum within ±1 s of the FRS peak time. (c) In this panel we plot δT_{ScS} for every geographic bin in our study region. In this plot, we used the tomography model S40RTS to calculate the reference times. There are more geographic bins shown in this panel than the other two, because we can calculate δT_{ScS} for a larger epicentral distance range than we can compute the FRS traces. (d) Inferred ULVZ thickness is shown for a fixed *S*-wave velocity decrease of 20 per cent. In each panel, specific geographic bins are numbered. The FRS traces for these numbered bins are shown in Fig. 13. The area with the best evidence for ULVZ presence is outlined with the red dashed line.

colour, whereas the symbol size is scaled by the amplitude of the peak. If a multiplication trace did not show a minimum within ±1 s of the FRS peak, we did not further consider that observation and plot a grey square. Select FRS traces (indicated by numbers 1–4 in Fig. 12), multiplication traces and forward and reverse traces are shown in Fig. 13 and discussed below. For reference, all FRS and multiplication traces are shown in Figures S37-S38. The area in the northwest of our study region (area approximated with red dashed lines in Fig. 12) shows the FRS traces with the largest amplitudes and largest time to the FRS maximum. In this region we see a maximum FRS trace amplitude of 0.27 and a maximum time to the FRS peak of 6.9 s. In the southeastern portion of our study region,

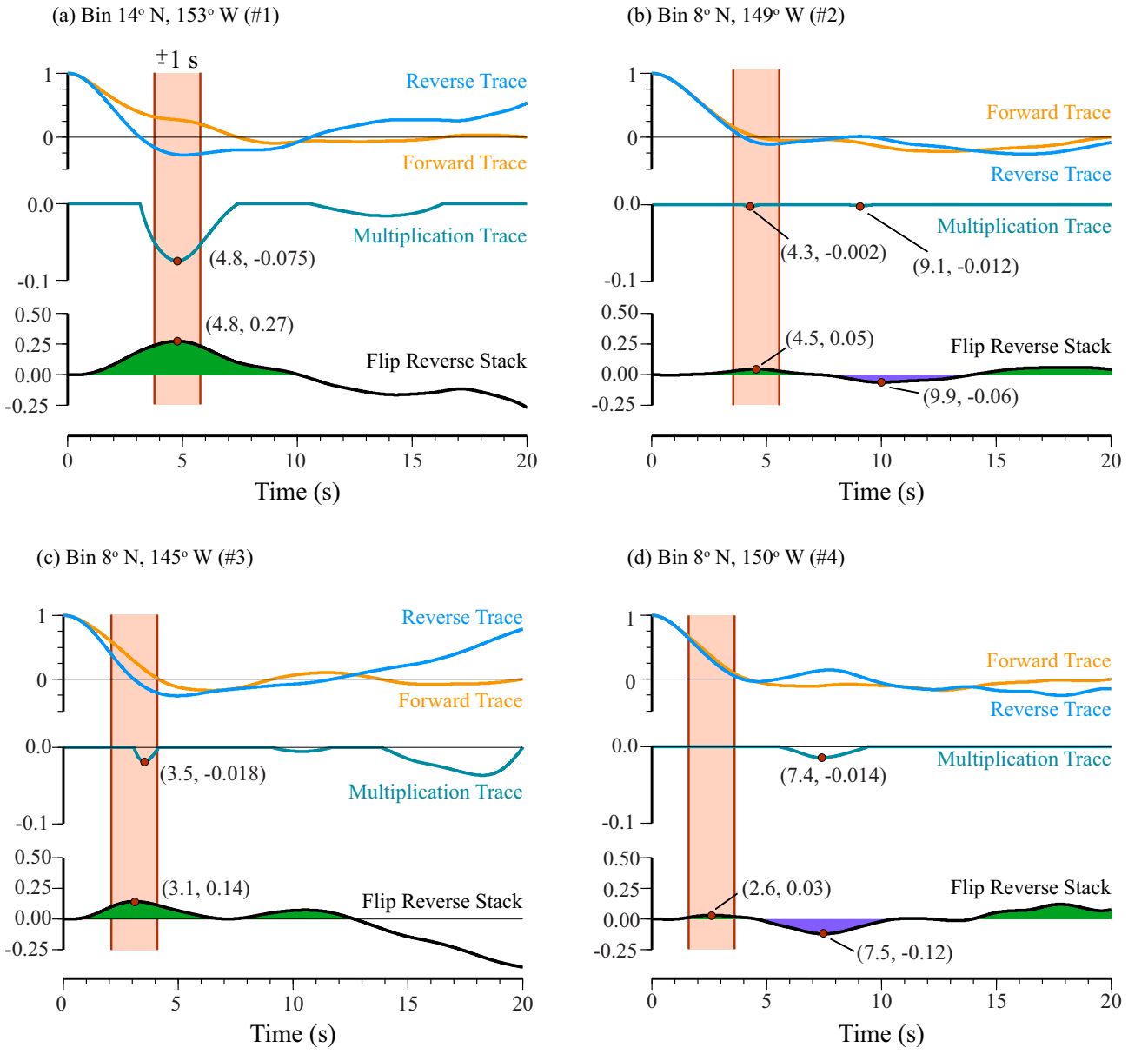

Figure 13. Traces are shown for geographic bin centres of (a) 14° N, 153° W, (b) 8° N, 149° W, and (c) 8° N, 145° W, and (d) 8° N, 150° W. Shown in each panel from top to bottom: the forward (orange) and reverse (light blue) traces, the multiplication trace (teal), and the FRS trace (black with positive portion filled in green. In panels b and d, where evidence for high velocity layering exists, the negative portion of the FRS traces are filled in purple. The peak of the FRS trace and multiplication traces are indicated by the red dots and the respective time and amplitudes are shown next to the traces. A window that is ± 1 s around the peak of the FRS trace is indicated in light red. The forward and reverse traces shown here are stacked from all traces occurring in the geographic bins.

we typically observe lower amplitude FRS traces (maximum amplitude = 0.14) that occur at earlier times (maximum time to FRS peak is 5.1 s).

The amplitude of the multiplication trace minima is shown in Fig. 12(b). Here we see that the largest magnitude multiplication traces correspond with the northwestern portion of our study region (red dashed lines) where we observe the largest amplitude FRS peaks. In the southeastern portion of our study region, we see extremely low amplitude peaks in the multiplication traces. This indicates that the strongest evidence for ULVZ existence occurs in the northwest of our study region.

In Fig. 12c we show δT_{ScS} for all geographic bins in our study region. Here we use traveltimes computed through tomography model S40RTS (Ritsema *et al.* 2011) to calculate T^{ref}_{ScS-S} in eq. (4). We also tested models SP12RTS (Koelemeijer *et al.* 2016) and SEMUCB-WM1 (French & Romanowicz 2015), but the results for all three models are similar (see Fig. S36). We can calculate δT_{ScS} for a larger number of geographic bins than we show in the previous two panels because we only need to be able to measure ScS and *S* traveltimes; whereas to calculate the FRS trace we need 10–15 s ahead of ScS that is free of direct *S* or SdS arrivals that may interfere with the calculation of the FRS trace. What we observe is that δT_{ScS} is positive between roughly 3 and 8 s across the entire study region, even after correcting for tomography. But the largest δT_{ScS} values do not correlate well with the region where we see the strongest ULVZ evidence (red dashed line) from the FRS and multiplication

traces. It is already known that tomography models do not capture the full extent of traveltime variations in this region and that the Pacific LLVP alone cannot explain excess traveltime delays in this region (Thorne *et al.* 2013b). Unfortunately, we cannot see a clear positive trend in δT_{ScS} as observed in the synthetic tests from the previous sections. Rather we can only say that traveltimes of arrivals passing through this complicated region are highly variable and up to several seconds of δT_{ScS} could be attributable to ULVZ existence, although it is unlikely that ULVZs are responsible for the full δT_{ScS} anomaly observed here.

Using the WKBJ method we computed synthetic seismograms for ULVZ models with *S*-wave velocity reductions from 1 to 40 per cent (in 1 per cent increments), thicknesses from 1 to 40 km (in 1 km increments), with density fixed at +5 per cent. We computed these synthetics specifically for the 22 October 2008 event, using a 233 km source depth and focal mechanism obtained from the NEIC. We computed synthetics along the average source–receiver azimuth (azimuth = 43°, Fig. 11b) for epicentral distances from 74° to 86° in 1° increments. All synthetics were convolved with the empirical *S*-wave source as described previously. Then, for each geographic bin we inferred ULVZ characteristics by the fitting method as described in Section 2. As observed in the synthetic tests, we find best-fitting models with a wide amount of uncertainty, due to the trade-offs between *S*-wave velocity and thickness. Rather than report on the best-fitting model, with variable *S*-wave velocity and thickness, we fixed the *S*-wave velocity reduction and found the best-fitting ULVZ thickness for that velocity decrease. An example, where the *S*-wave velocity is fixed at −20 per cent is shown in Fig. 12(d). We see that these observations support a generally thicker ULVZ to the northwest (up to 9 km thick, for $\delta V_S = -20$ per cent) than for the southeast which generally gives thicknesses from 2 to 5 km. The goodness of fit as a function of *S*-wave velocity and thickness is shown in Fig. S39. As discussed with the synthetic examples there is an apparent greater constraint on ULVZ thickness than on *S*-wave velocity contrast, so long as the *S*-wave velocity contrast is greater than approximately 10 per cent where the corner in the trade-off curve exists. For example, for *S*-wave velocity contrasts between −10 and −40 per cent the best-fitting ULVZ thickness could vary from 4 to 14 km. But for smaller magnitude velocity contrasts (<10 per cent) the best-fitting ULVZ thickness could vary from 14 to 40 km.

Example FRS and multiplication traces, along with forward and reverse traces are shown in Fig. 13. Here we show four examples (numbered 1–4, which are labelled in Fig. 12). The first example, (#1–Fig. 13a) shows a geographic bin in the northwest that shows good evidence for ULVZ presence. The forward and reverse traces (orange and blue traces respectively) show evidence for opposite polarities which is manifest by a large negative peak in the multiplication trace (cyan line). This minimum in the multiplication trace corresponds well with the peak in the FRS trace. Most of the traces in the immediate vicinity of this example bin look similar (Fig. S38) and are excellent candidates for ULVZ existence.

The second example (#2, Fig. 13b) shows an extremely low amplitude FRS trace (amplitude = 0.05 relative to ScS). Although a minimum appears in the multiplication trace, its magnitude is quite low (−0.002). This bin shows almost no evidence for ULVZ existence. Data in this bin also shows a positive amplitude precursor about 10 s ahead of ScS that can be seen in the raw waveforms (see Fig. 11c at distances between roughly 75° and 77°). It is possible that this could indicate a high velocity layer that is higher up from the CMB. There is a low amplitude minimum in the multiplication trace at about 9 s, which is close to a negative peak in the FRS trace around 10 s. The neighbouring bin (8° N and 150° W -see Fig. 13d) also shows a similar feature. But the waveforms show a positive peak in the reverse trace and not a notable negative peak in the forward trace. As such this arrival could be an Scd arrival from a *D″* discontinuity. None of the UHVZ models tested in this paper generates a precursor that is 10 s ahead of ScS, indicating that high velocity layering must be greater than 40 km thick to generate this arrival. We do not perform waveform modelling to determine the thickness of *D″* discontinuity that would be inferred by this arrival. But this is generally consistent with a *D″* discontinuity arrival as discussed below in Section 6.2.

The third example (#3, Fig. 13c) shows stronger evidence for mild ULVZ existence in the southeastern portion of the study region. Here we see a lower FRS amplitude of 0.14 (relative to ScS) which is about half of the FRS amplitudes in the northwest, but subtle increases in amplitude of the forward trace relative to the reverse trace give a noticeable minimum in the multiplication trace. Such an observation could be at the limits of what is resolvable using the FRS method.

The fourth example (#4, Fig. 13d) shows a case where we do not observe a minimum in the multiplication trace near the time of the FRS peak. There is only a low amplitude peak in the FRS trace (amplitude = 0.03), and almost no difference between forward and reverse traces, resulting in no observable minimum in the multiplication trace in the vicinity of the FRS peak time. This observation shows no evidence for ULVZ existence. As noted above, a potential high velocity layer, could be indicated in this bin as well.

Taking all of the above discussion into consideration, we conclude the following about ULVZ presence in this area.

(i) The best evidence for ULVZ presence is in the northwest of the study region, centred near 14°N and 153°W.

(ii) From the data we have collected, this ULVZ may be approximately 4° × 6° (∼250 km × 360 km) in lateral scale. But we do not have data on all sides of this ULVZ, so it could be larger.

(iii) From these data we cannot uniquely constrain *S*-wave velocity. If the *S*-wave velocity is fixed, we can estimate ULVZ thickness. If we fix δV_S at −20 per cent, then the ULVZ thickness varies from 7 to 9 km. But, fixing δV_S at a smaller reduction of −10 per cent would imply a 9–16-km-thick ULVZ.

(iv) There is little evidence for ULVZs in the majority of the southeastern part of our study region. Nevertheless, near 8°N and 145°W, there is additional ULVZ evidence. If we fix δV_S at −20 per cent, this would imply a thin 4–5-km-thick ULVZ in this region.

(v) At 8°N and −151° to −150°W there are subtle negative peaks in the FRS and multiplication traces that could be consistent with a high velocity interface (*D″* discontinuity).

6 DISCUSSION

6.1 ULVZ detection to the southeast of Hawaii

We see the strongest ULVZ evidence in the northwestern part of our study area centred around 14°N and 153°W. Several previous studies have inferred ULVZ presence in the same location we investigate in this study. Two studies have inferred ULVZ presence based on ScS waveforms. Zhao *et al.* (2017) models a ULVZ here with substantially larger perturbations of $\delta V_S = -30$ per cent with

a thickness of 20 km. This result could be due to constructive interference with arrivals generated from a thin D'' discontinuity arrival. This possibility is discussed further in Section 6.2. On the other hand, assuming a velocity reduction between 10 and 30 per cent Jenkins *et al.* (2021) finds that the ULVZ located here must range in thickness between 3 and 15 km, which is nearly identical to our measurements.

Adjacent to the region we investigated on the northeast side, Sun *et al.* (2019) used ScS traveltimes and waveforms to infer an 85 km thick ULVZ with a 15 per cent reduction in *S*-wave velocity. We cannot verify this large ULVZ thickness from data we used in this study. It is possible that the ULVZ we image in this study is a part of a much larger structure as inferred by Sun *et al.* (2019). Nonetheless, data used in that study appear to show symmetrical ULVZ-related precursors and would be good candidate data to further explore using the FRS method.

In the southeastern portion of study region (centred around 9°N and 147°W) we observed weak to no ULVZ presence. However, several studies argue for ULVZs in this location. Avants *et al.* (2006a) infers a 24–30 km thick low velocity zone with δV_S varying from −3.3 to −7.4 per cent. Because the trade-offs between thickness and *S*-wave velocity are so large, these values are within the possibilities of reasonable models we find for some of our geographic bins (e.g. 8°N and 145°W). Though we note that study was based on 1-D modelling assumptions. Liu *et al.* (2011) also infers ULVZ presence here, but does not state what ULVZ parameters best-fitting their observations. Lai *et al.* (2022) finds a ULVZ with 30 km thickness and 18 per cent *S*-wave velocity reduction southeast of the area we investigate. It is possible what we see in the far southeast of our study trends into a larger ULVZ as inferred by Lai *et al.* (2022). However, Wolf & Long (2023) finds a 6° diameter ULVZ centred at 8°N, 150°W with a 20 per cent *S*-wave velocity reduction and a thickness of 10 km based on Sdiff post-cursors. This is exactly centred on a region where we see the weakest evidence for ULVZs anywhere in our study. It is unclear why this discrepancy between the ScS arrivals and the Sdiff arrivals exists, though we note that Sdiff imaging requiring strong ULVZs may have trouble precisely pinpointing structures along the great-circle path direction, and have a finite frequency sensitivity over a significantly larger volume than ScS. Thus, the structure affecting Sdiff in Wolf & Long (2023) may be in a slightly shifted position.

6.2 D'' discontinuity interference

Care must be taken to not use data where SdS arrivals associated with the D″ discontinuity may interfere with the ScS precursory wavefield. This may be particularly relevant for the larger epicentral distances (nearing 80°) where the negative down swing of the phase shifted Sbc arrival due to the D'' discontinuity may constructively interfere with the SdS ULVZ arrival. This could result in a spurious ULVZ detection or, if a ULVZ does exist, could increase the amplitude of the FRS trace. Plotting a distance profile such as those shown in Fig. 11 can assist in identifying when arrivals associated with a D'' discontinuity exist and should be consulted for each event.

Example synthetics with both a D'' discontinuity and ULVZ are shown in Fig. 14. Waveforms are shown in Fig. 14(a) as a function of epicentral distance (Δ). At the shortest distance ($\Delta = 70°$) the Scd arrival from the D'' discontinuity is well separated from ScS and the SdS arrival generated by the ULVZ. For this distance we can see a separate positive polarity peak in the FRS trace for the ULVZ and negative polarity peak for the D'' discontinuity. But for increasing epicentral distances the D'' discontinuity Scd arrival enters closer in time to the ScS and SdS ULVZ arrivals. This has the effect to artificially increase the amplitude and delay the time of the FRS peak. Thus, if data are considered in FRS modelling that are too close in time to potential D'' discontinuity arrivals it may act to enhance the FRS peaks. It is not clear if previous FRS studies have considered this potential effect. This may be especially important in the vicinity of the LLVPs where the D'' discontinuity may lie closer to the CMB and consequently the D'' discontinuity arrivals are closer in time to the ScS arrival (e.g. Garnero *et al.* 1993; Sidorin *et al.* 1999; Lay *et al.* 2006; Takeuchi & Obara 2010).

6.3 Box-car versus Gaussian shaped ULVZ geometries

Pachhai *et al.* (2024) examined 2.5-D ULVZ waveform effects for short period ScP arrivals. This study investigated waveform effects from box-car and Gaussian shaped ULVZs as well as an intermediary form defined by a Tukey function. The box-car shaped ULVZs produced the most severe ScP multipath arrivals, similar to the ScS multipath arrivals observed in this study for box-car shaped ULVZ and UHVZ models. In the box-car ULVZ models of Pachhai *et al.* (2024) the dual ScP arrivals were both impulsive and distinctive due to the sharp ULVZ boundary. The Gaussian shaped ULVZs showed the most subdued multipath arrivals, whereas the Tukey function models showed waveforms intermediary between the Gaussian and box-car shaped ULVZs. All model types (Gaussian, Tukey and box-car) showed extra post-cursor arrivals associated with the boundaries of the finite length ULVZ models. Of the models explored, the box-car shaped ULVZs exhibited the most distinct multipath arrivals and were the most challenging to model. Large scale ($l = 12°$) Gaussian shaped models were more readily recovered with inversion techniques based on 1-D waveform modelling. Thus, it may be possible that the box-car shaped models presented in this study, represent the worst-case scenario for recovering ULVZ and UHVZ parameters.

Here we test a Gaussian shaped ULVZ model with a length of $l = 12°$, a maximum height of $h_{\max} = 20$ km, and $\delta V_S = -20$ per cent. We define the ULVZ anomaly as a function of angular distance from the source (θ):

$$h(\theta) = h_{max} e^{-\frac{1}{2}\left(\frac{\alpha\pi}{l}\right)^2}, \tag{5}$$

where $\alpha = l_1 + \frac{l}{2} - \theta$.

Waveforms for the Gaussian shaped ULVZ (red traces) are overlain on the corresponding box-car shaped synthetic waveforms (grey traces) in Fig. 15(a). The most important differences between the two are that in the waveforms for the Gaussian model we do not see two distinct ScS arrivals at the ULVZ boundaries ($l_1 = 28°$ and $l_1 = 34°$), but we primarily see an ScS arrival with either PREM (ScS^P) or ULVZ-like (ScS^U) arrival times depending on whether or not it travelled through the ULVZ. Furthermore, the amplitude of the extra post-cursory wavefield arrivals is lower for the Gaussian shaped ULVZ models. Indeed, at the largest ULVZ edge positions (e.g. $l_1 \geq 38°$) we see little post-cursory energy at all in the Gaussian models compared to the box-car shaped models.

In Figs 15(b) and (c) we show the ULVZ parameters recovered by the fitting method of Zhao *et al.* (2017) for the Gaussian shaped ULVZ models. Similar to the box-car shaped models there is still large trade-offs between thickness and *S*-wave velocity resulting in large uncertainty in recovered parameters. δT_{ScS} shows increased

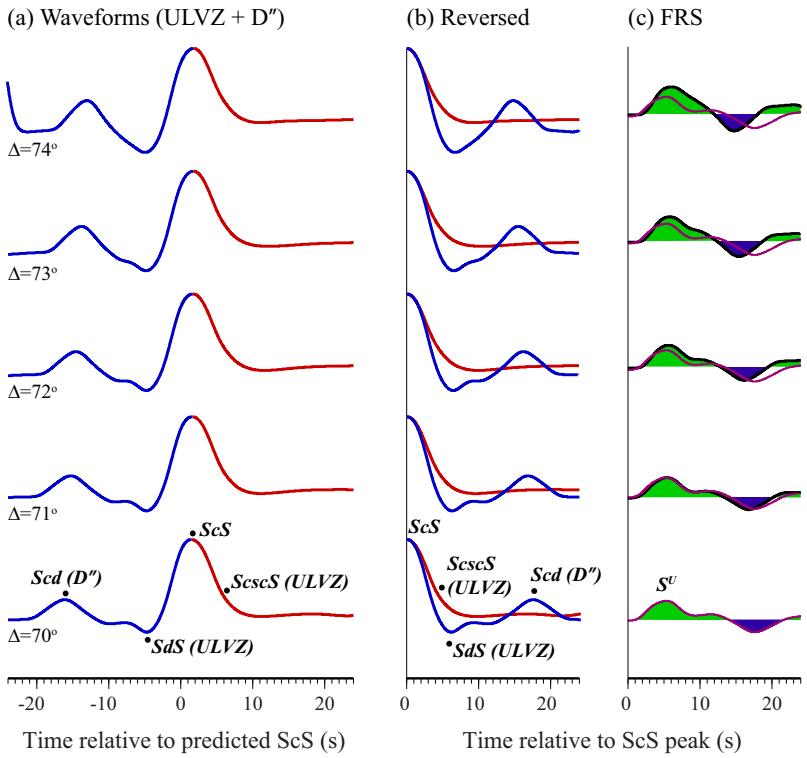

Figure 14. (a) Waveforms for a 1-D model with both a D″ discontinuity and ULVZ. Each trace is for a different epicentral distance ranging from 70° to 74° in 1° increments. All traces are transverse component displacement seismograms aligned on the PREM predicted ScS arrival time. The forward trace is drawn in red while the reverse trace is drawn in blue. Synthetics are convolved with the source-time function of the Oct. 22, 2008 event. (b) The reverse trace is time reversed and overlaid on top of the forward trace. (c) The FRS traces are shown. The FRS trace for Δ=70° is drawn in red and repeated for each epicentral distance. The positive and negative portions of the FRS trace are filled in green and purple respectively. The D″ discontinuity model has 2 per cent S-wave velocity increase 250 km above the CMB. The ULVZ model has a 20 per cent S-wave velocity decrease with a thickness of 20 km.

values for edge positions situated such that the ScS bounce point is directly beneath the maximum ULVZ thickness. The multiplication traces for the Gaussian shaped model are simpler than for the box-car shaped model, and we observe well defined opposite polarity arrivals for the interior of the ULVZ. The reduced complexity of the Gaussian shaped ULVZ models could be more similar to what is encountered in the Earth, however, even in this case there is additional post-cursory wavefield complexity not encountered in 1-D ULVZ models.

6.4 Interpretation of FRS traces

The FRS traces computed for the 2.5-D ULVZ and UHVZ models presented in this paper show strong peaks and troughs that are not present in 1-D models. Previous studies using the FRS technique have attempted to model multiple peaks in the FRS traces resulting in multilayer ULVZ models (e.g. Zhao *et al.* 2017). However, it is possible that structure from a single layer ULVZ with finite length is responsible for some of the FRS trace complexity. To highlight the complexity, we show the FRS traces (black traces) for a ULVZ model with $l = 6°$, $h = 20$ km and $\delta V_S = -20$ per cent in Fig. 16. The inspiration for this figure was drawn from Jenkins *et al.* (2021) which shows intriguing complexity in the FRS traces as a function of distance across the CMB. In this plot we shade the positive and negative portions of the FRS trace as red and blue respectively. For this finite length ULVZ model, the ULVZ position exists between roughly 1700 and 2050 km. For these locations inside of the ULVZ we see a negative down swing, followed by the main positive FRS peak at about 5 s, followed by an additional peak about 4 s later. On the ULVZ edges we observe a broad positive peak in the FRS arrival at about 3 s which is also followed by another positive peak at about 9 s. Additional, diffracted-like peaks are observable in the FRS traces on either side of the ULVZ. In these locations, away from the ULVZs, multiple peaks may be observable in the FRS traces. Because of multiple peaks exist in the FRS traces from a single layer, yet finite length ULVZ, it is advisable for FRS studies to not model more than the primary FRS peak and to be cautious of interpreting more of the peaks as layered ULVZ structure. The corresponding multiplication traces are shown in Fig. 16(b). The multiplication traces show lower amplitude variability in the regions outside of the ULVZ and in the times that are later than the primary FRS peak time. This demonstrates that the multiplication trace can be useful in the interpretation of where ULVZs exist. However, the ULVZ boundaries are dominated by the largest amplitude multiplication trace amplitudes due to the ScS multipath arrivals.

6.5 Deconvolution and trade-offs

All previous studies using the FRS technique have stacked data from multiple events together to create the FRS traces. This was accomplished through a deconvolution process to normalize differences in event source-time functions (Zhao *et al.* 2017; Fan & Sun 2021; Jenkins *et al.* 2021; Fan *et al.* 2022). However, challenges exist in deconvolution approaches due to increased noise levels introduced into the deconvolved seismic traces (e.g. Kelly & Lines 1994). In this study, we have only used synthetics and single events at a time,

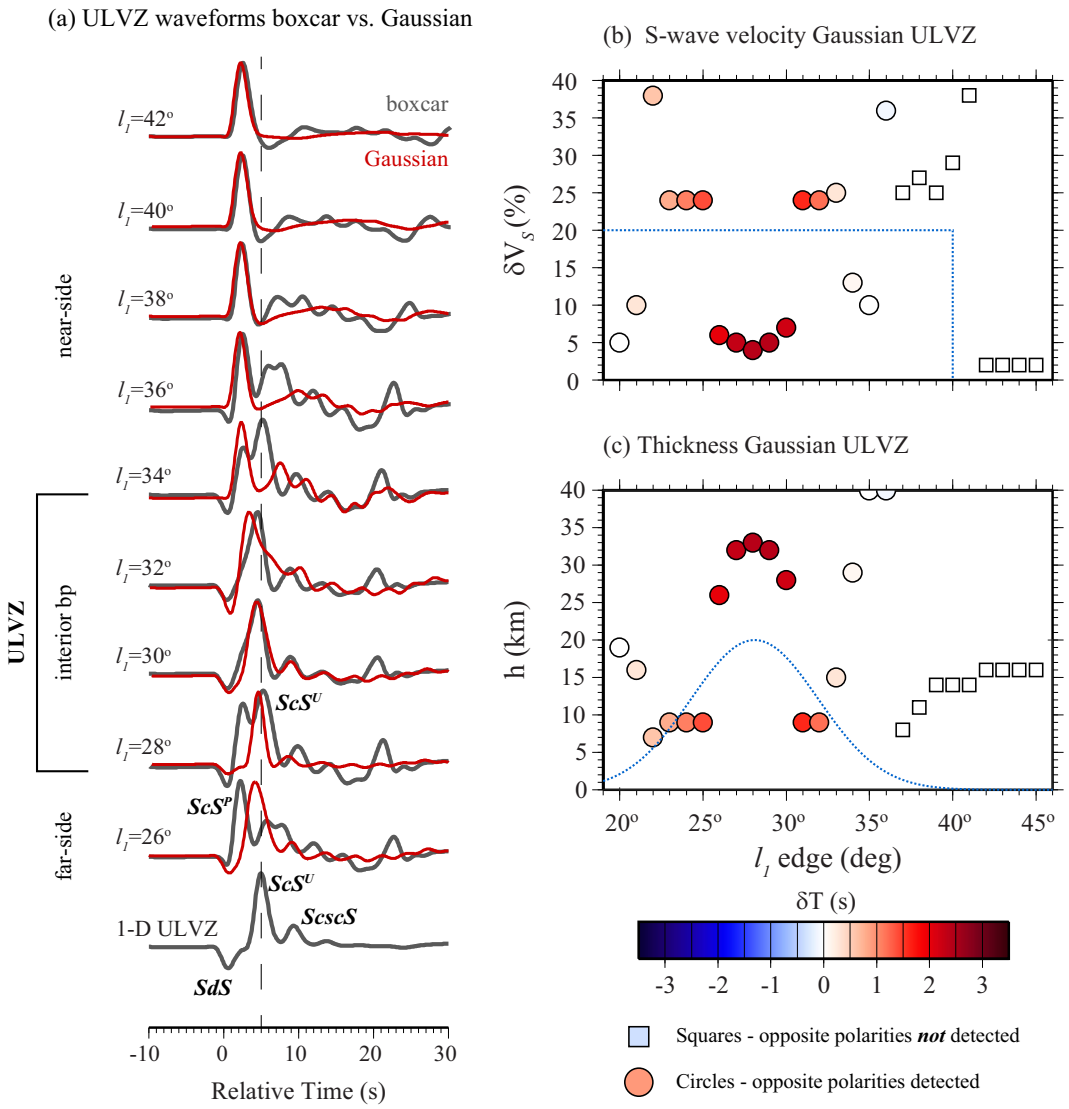

Figure 15. (a) A comparison of waveforms for box-car shaped ULVZ models (grey traces) and Gaussian shaped ULVZ models (red traces) as a function of ULVZ edge positions from $l_1 = 26°$ to $l_1 = 42°$). Waveforms are for a ULVZ model with $\delta V_S = -20$ per cent and maximum thickness of $h_{\max} = 20$ km. The lowermost trace in this panel is for the corresponding 1-D ULVZ model. Transverse component displacement traces are shown aligned in time on the PREM predicted ScS arrival time. (b) Recovered *S*-wave velocity for the Gaussian shaped ULVZ using the fitting method of Zhao *et al.* (2017). The expected *S*-wave velocity is shown by the dashed blue line. Symbols are shaded by δT_{ScS} and are drawn as either circles or squares depending on whether the multiplication traces detected opposite polarity arrivals in the forward and reverse traces. (c) Same as panel (b) except for ULVZ thickness.

and thus have avoided deconvolution pitfalls. Future FRS studies could potentially avoid deconvolution by modelling single events at a time. Instead of stacking all events together and then modelling a single FRS trace, individual events could be modelled independently with modelled likelihood functions for each event combined through the product of likelihoods (e.g. see Pachhai *et al.* 2023 as applied to ScP waveforms). Such an approach may also help to reduce some of uncertainties due to the strong trade-offs (Pachhai *et al.* 2023).

6.6 Resolution limits for ULVZ detection

An interesting question is how thick of a ULVZ can be detected using the FRS method. In reflection seismology the thickness of a bed that can be detected depends on being able to detect a second reflected arrival and theoretically can be as small as 1/8 the wavelength of the seismic waves being used (e.g. Widess 1973; Brown & Thorne 2013). However, with the FRS technique, we are stacking opposite sides of the ScS waveform and detection is potentially sensitive to minor changes in the width of the waveform. To explore the ULVZ resolution limit, we compute a series of synthetic seismograms for 1-D ULVZ models using the full waveform SHaxi method. We compute models for both the weak ($\delta V_S = -5$ per cent) and strong ($\delta V_S = -20$ per cent) cases, with ULVZ thicknesses from 1 to 12 km in 1 km increments. We used a dominant period of 6 s in these calculations to be consistent with typical SH-wave recordings. Synthetic seismograms, forward and reverse traces, FRS and multiplication traces for all ULVZ thicknesses are provided in Figs S40–S41. It is evident in these figures that there is a general increase in amplitude of the FRS peak with increasing ULVZ thickness. For the strong case ($\delta V_S = -20$ per cent) this amplitude increase begins to

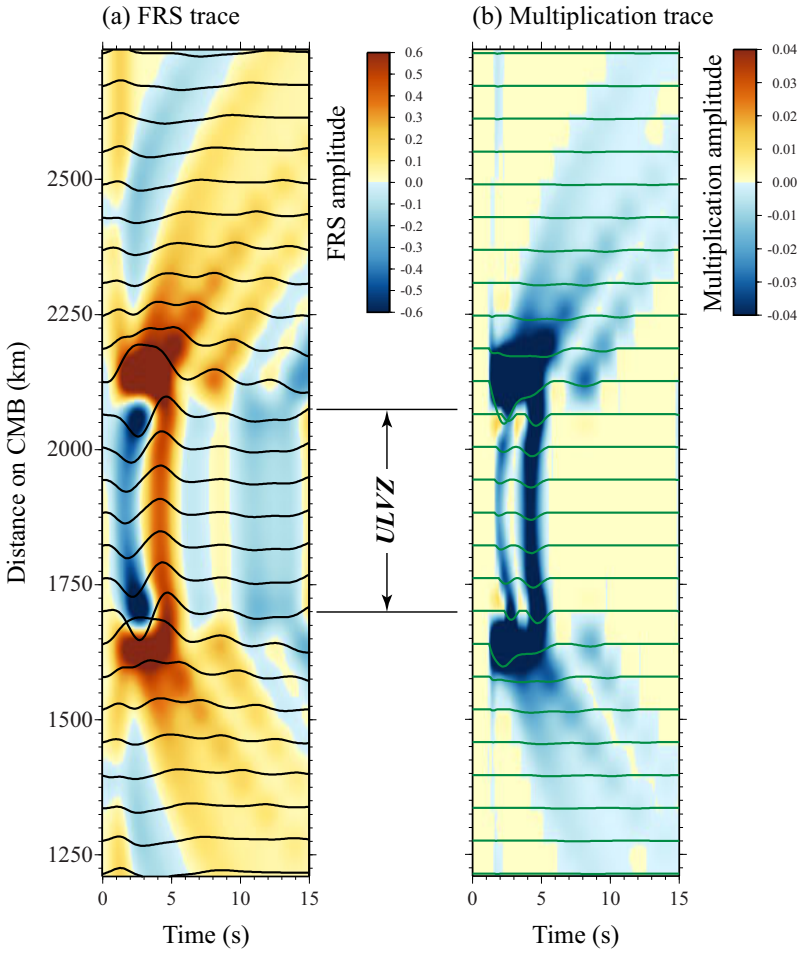

Figure 16. (a) FRS traces as a function of distance along the CMB for ULVZ models with $h = 20$ km, $\delta V_S = -20$ per cent and $l = 6^\circ$. Black lines show the FRS traces for each edge position from $l_1 = 20^\circ$ (bottom of plot) to $l_1 = 45^\circ$ at the top of the plot. The positive amplitudes are shaded in red and the negative amplitudes are shaded in blue. (b) Multiplication traces corresponding to the FRS traces shown in panel (a).

flatten out for ULVZ thicknesses greater than 9 km. Furthermore, the magnitude of the multiplication trace peak amplitude also increases with increasing ULVZ thickness. If we used a detection threshold of −0.01 on the multiplication trace, as done in our previous tests in this paper, then we can see a detectable FRS peak and multiplication trace for ULVZ thicknesses above 9 km for the weak case ($\delta V_S = -5$ per cent) and above 4 km for the strong case ($\delta V_S = -20$ per cent). In the lowermost mantle this corresponds to roughly 1/5 and 1/10 of the wavelength for each case respectively. This detection limit depends on the *S*-wave velocity decrease in the ULVZ and even thinner ULVZs could potentially be detected for larger *S*-wave velocity contrasts.

Yet, real seismic data is noisy, so we also considered adding random noise to our synthetic seismograms (see e.g. Pachhai *et al.* 2022b). We did this by convolving a Gaussian autocorrelation function (ACF) with 50 unique series of random numbers where we defined the ACF as:

$$ACF(t) = \sigma e^{-t^2/T_c^2}, \tag{6}$$

where σ is the root-mean square of the noise relative to the direct *S* wave, and T_c is the corner period. We used corner periods of $T_c = 0.5$, 1.0 and 5.0 s and $\sigma = 0.01$ which is comparable to good quality observations (seismograms for these noisy cases are shown in Figs S42–S47 for each corner period and *S*-wave velocity decrease). The FRS peak amplitudes and multiplication trace amplitudes are shown for the weak ($\delta V_S = -5$ per cent) and strong ($\delta V_S = -20$ per cent) cases in Figs S48 and S49, respectively. In these figures, we show the mean and standard deviation of the peak values for the 50 random realizations of noise. The results are largely independent of the noise corner period (T_c) but for the weak case there is a noticeable average increase in FRS peak amplitude for added short period noise that is not mimicked in the multiplication trace amplitude, providing additional evidence for the utility of consulting the multiplication trace. Again, using a detection threshold of −0.01 we can see that we are above the detection threshold for ULVZ thicknesses above 12 km (roughly 1/4 wavelength) for the weak case, and above 5 km (roughly 1/10 wavelength) for the strong case. Here we define being above the detection threshold if all observations within one standard deviation are below the -0.01 multiplication trace threshold. We note that in real data observations in this study, we stack a minimum of 15 seismic traces gaining excellent SNR improvement that is at least comparable or better than the noisy data shown in this study. Nonetheless, with a velocity decrease of 20 per cent the best we can expect to resolve is a ULVZ with a thickness of about 4–5 km thickness. Thus, if ULVZ material exists in the southeast region of our study, it is likely at, or below, our detection limit.

6.7 Detection of UHVZs

Detection of UHVZs with ScS analyses may be especially challenging using FRS. As shown in Fig. 2(d), a thin (10 km) UHVZ with a 10 per cent increase in *S*-wave velocity shows almost no waveform perturbation and would not be detectable using the FRS technique. An even larger UHVZ (e.g. 20 km thick) may be exceptionally problematic for interpretation of CMB structure. In this case, there is only a small perturbation in the wavefield that could potentially be detected using the FRS technique. The waveform itself looks remarkably similar to an ScS arrival, and in real data would most likely be interpreted as such. However in reality, this is an Sbc reflection 20 km above the CMB and not an ScS arrival at all. This could have potential for misinterpretation of arrivals that go into global tomography models. But the end result is to make UHVZs nearly invisible to those seeking to interpret the ScS wavefield for all but the most extreme UHVZ cases. If a UHVZ is suspected, additional seismic arrivals could help in identification.

7 CONCLUSIONS

In this paper, we examined 1-D and 2.5-D models of ULVZ and UHVZ heterogeneities. 1-D ULVZ models show consistent precursor (SdS) and post-cursor (ScscS) arrivals approximately symmetrical in time around the ScS arrival, but with opposite polarities. 2.5-D ULVZ models are more complicated and depend on the lateral dimensions of the ULVZ as well as the ScS bounce point location with respect to the ULVZ. Additional ScS multipath arrivals and post-cursor arrivals may exist within a few 10 s of seconds of the ScS arrival. Importantly, ScS post-cursors may exist even when the ScS ray path does not directly strike the ULVZ from above. In this case, one might observe post-cursors that manifest in a positive FRS peak, leading to mistaken ULVZ identification. Indeed, a challenge with the FRS method is in determining whether or not the ScS ray paths are directly striking the ULVZ. If they are not, then any subsequent modelling efforts using 1-D methods produce incorrect models. Using the time domain multiplication trace between the forward and reverse waveforms provides a method to help quantify where the symmetric opposite polarity arrivals exist, and hence when the ray paths are interacting with a ULVZ. In addition, tabulating positive δT_{ScS} values may support ULVZ identification. However, with real data this may be a challenge as current tomographic models do not predict ScS traveltimes well enough for some paths through the Earth. Additional care must be given as to whether or not arrivals generated from a D″ discontinuity (Scd + Sbc) exist. When the ScS arrival gets too close in time to these *D″* discontinuity arrivals, constructive interference may cause an increase in the amplitude of the negative polarity ScS precursor, resulting in a larger peak in the FRS trace. This may ultimately result in an overestimation of the ULVZ physical properties, if not in complete misidentification of ULVZ existence.

Synthetic predictions for 1-D UHVZ models offer unique complications. Depending on the UHVZ thickness and velocity contrast a variety of arrivals may be present in the vicinity of the predicted ScS arrival time which are not consistently pre- or post-cursor. To make matters worse, the ScS arrival itself may not always be present. With increasing UHVZ velocity contrast, ScS ray paths pass the critical angle, and the ScS arrival may disappear. However, the resulting waveform in such a case is dominated by a post-critical reflection off of the top of the UHVZ and may still strongly resemble an ScS waveform. For 2.5-D UHVZ models, additional waveform complexities also exist similar to those for ULVZ models. Namely, ScS mutlipathing may occur as well as the development of a complicated ScS coda. Again, this coda may exist even when the ScS ray path does not directly strike the UHVZ from above. Tabulating negative δT_{ScS} values and quantifying opposite polarity arrivals with the multiplication trace may be valuable tools in determining whether or not a direct interaction with the UHVZ has occurred.

Regardless of ULVZ or UHVZ heterogeneity, methods of matching the FRS peak time and amplitude are subject to strong trade-offs in modelled *S*-wave velocity and thickness. However, if the *S*-wave velocity decrease for ULVZs is larger than about 10 per cent, then the FRS peak constrains the ULVZ thickness with greater certainty. If the *S*-wave velocity contrast drops to low values, for example less than 5 per cent, then there is little constraint on thickness. Because of the additional ScS coda waves generated by finite length ULVZs or UHVZs, even for smooth Gaussian shaped models, it is advisable to avoid modelling multiple peaks in the FRS traces. We applied the knowledge we gained from examining the synthetic wavefield of 1-D and 2.5-D ULVZs and UHVZs to real data interacting with the lower mantle to the southeast of Hawaii. Here we find evidence that ULVZ heterogeneity does exist in this location with the strongest signal in FRS traces centred near 14°N and 153°W.

ACKNOWLEDGMENTS

We acknowledge the University of Utah Center for High Performance Computing (CHPC) for computing resources and support. We thank editor Sanne Cottaar, Jiewen Li and an anonymous reviewer for their thoughtful suggestions which helped improve this manuscript. MT and SP were partially supported by NSF grant EAR-2132400. EG was partially support by NSF grant EAR-1855624. Figures were drawn with the Generic Mapping Tools (Wessel *et al.* 2019). IRIS and SCEDC data used in this study were obtained with the SOD utility (Owens *et al.* 2004). The facilities of IRIS Data Services, and specifically the IRIS Data Management Center, were used to access the raw waveforms used in this study. IRIS Data Services are funded through the Seismological Facilities for the Advancement of Geoscience and EarthScope (SAGE) Proposal for the National Science Foundation under Cooperative Agreement EAR-1261681.

SUPPORTING INFORMATION

Supplementary data are available at *GJIRAS* online.

Figures S1–S12. Waveforms and FRS traces for ULVZ models.
Figure S13. Verification of WKBJ synthetics for ULVZ models.
Figures S14–S16. Waveform fitting results for ULVZ models.
Figures S17–S18. 1-D UHVZ model tests.
Figures S19–S20. 2.5-D UHVZ model sensitivity tests.
Figures S21–S32. Waveforms and FRS traces for UHVZ models.
Figures S33–S35. Waveform fitting results for UHVZ models.
Figure S36. Tomography corrections.
Figures S37–S38. FRS stacks and multiplication traces for example data.
Figure S39. Example trade-off curve for data.
Figures S40–S49. ULVZ thickness resolution.

Please note: Oxford University Press is not responsible for the content or functionality of any supporting materials supplied by the

authors. Any queries (other than missing material) should be directed to the corresponding author for the paper.

DATA AVAILABILITY

Seismic recordings for the 22 October 2008 event and full waveform 2.5-D synthetic predictions for UHVZ models analysed in this study are available for download from the hive.utah.edu data repository (https://doi.org/10.7278/S5d-gsmt-m8bc).

REFERENCES

Andrault, D., Pesce, G., Bouhifd, M.A., Bolfan-Casanova, N., Hénot, J.-M. & Mezouar, M., 2014. Melting of subducted basalt at the core-mantle boundary, *Science,* **344,** 892–895.

Avants, M., Lay, T. & Garnero, E.J., 2006a. A new probe of ULVZ S-wave velocity structure: array stacking of ScS waveforms, *Geophys. Res. Lett.,* **33,** doi:10.1029/2005GL024989.

Avants, M., Lay, T., Russell, S.A. & Garnero, E.J., 2006b. Shear velocity variation within the D" region beneath the central Pacific, *J. geophys. Res.,* **111,** doi:10.1029/2004JB003270.

Borgeaud, A.F.E., Kawai, K., Konishi, K. & Geller, R.J., 2017. Imaging paleoslabs in the D" layer beneath Central America and the Caribbean using seismic waveform inversion, *Sci. Adv.,* **3,** 1–10.

Brown, S.P. & Thorne, M.S., 2013. Viterbi sparse spike detection, *Geophysics,* **78,** V157–V169.

Brown, S.P., Thorne, M.S., Miyagi, L. & Rost, S., 2015. A compositional origin to ultralow-velocity zones, *Geophys. Res. Lett.,* **42,** 1039–1045.

Buffett, B.A., Garnero, E.J. & Jeanloz, R., 2000. Sediments at the top of Earth's core, *Science,* **290,** 1338–1342.

Chapman, C.H. & Orcutt, J.A., 1985. The computation of body wave synthetic seismograms in laterally homogeneous media, *Rev. Geophys.,* **23,** doi:10.1029/rg23i002p00105.

Cobden, L., Thomas, C. & Trampert, J., 2015. 13 Seismic detection of post-perovskite inside the Earth, in *The Earth's Heterogeneous Mantle,* pp. 391–440, eds, Deschamps, F. & Khan, A., Springer Geophysics.

Cottaar, S., Martin, C., Li, Z. & Parai, R., 2022. The root to the Galapagos mantle plume on the core-mantle boundary, *Seismica,* **1,** 1–12.

Cottaar, S. & Romanowicz, B., 2012. An unusually large ULVZ at the base of the mantle near Hawaii, *Earth planet. Sci. Lett.,* **355-356,** 213–222.

Crotwell, H.P., Owens, T.J. & Ritsema, J., 1999. The TauP Toolkit: flexible seismic travel-time and ray-path utilities, *Seismol. Res. Lett.,* **70,** 154–160.

Cummins, P.R., Takeuchi, N. & Geller, R.J., 1997. Computation of complete synthetic seismograms for laterally heterogeneous models using the Direct Solution Method, *Geophys. J. Int.,* **130,** 1–16.

Dannberg, J., Myhill, R., Grassmöller, R. & Cottaar, S., 2021. The morphology, evolution and seismic visibility of partial melt at the core-mantle boundary: implications for ULVZs, *Geophys. J. Int.,* **227,** 1028–1059.

Dziewonski, A.M. & Anderson, D.L., 1981. Preliminary reference Earth model, *Phys. Earth planet. Inter.,* **25,** 297–356.

Fan, A. & Sun, X., 2021. Origin of ULVZs near the African LLSVP: implications from their distribution and characteristics, *Earthq. Sci.,* **34,** 299–309.

Fan, A., Sun, X., Zhang, Z., Zhang, P. & Zong, J., 2022. From subduction to LLSVP: the core-mantle boundary heterogeneities across North Atlantic, *G-cubed,* **23,** 1–12.

Festin, M.M., Thorne, M.S. & Li, M., 2024. Evidence for ultra-low velocity zone genesis in downwelling subducted slabs at the core-mantle boundary, *Seismic Record,* **4,** 111–120.

French, S.W. & Romanowicz, B., 2015. Broad plumes rooted at the base of the Earth's mantle beneath major hotspots, *Nature,* **525,** 95–99.

Frost, D.A., Rost, S., Garnero, E.J. & Li, M., 2017. Seismic evidence for Earth's crusty deep mantle, *Earth planet. Sci. Lett.,* **470,** 54–63.

Fuchs, K. & Müller, G., 1971. Computation of synthetic seismograms with the reflectivity method and comparison with observations, *Geophys. J. R. astr. Soc.,* **23,** 417–433.

Garnero, E., Yu, S., Shim, S.-H., Li, M., Ko, B., Thorne, M.S. & Zhao, C., 2020. Ultra high velocity zones at the core-mantle boundary, in *Proceedings of the AGU Fall Meeting Abstracts,* Online, 1–17 December, AGU.

Garnero, E.J., Helmberger, D.V. & Grand, S.P., 1993. Preliminary evidence for a lower mantle shear wave velocity discontinuity beneath the central Pacific, *Phys. Earth planet. Inter.,* **79,** 335–347.

Garnero, E.J. & Jeanloz, R., 2000. Fuzzy patches on the earth's core-mantle boundary?, *Geophys. Res. Lett.,* **27,** 2777–2780.

Garnero, E.J. & Vidale, J.E., 1999. ScP; a probe of ultralow velocity zones at the base of the mantle, *Geophys. Res. Lett.,* **26,** 377–380.

Gassner, A., Thomas, C., Kruger, F. & Weber, M., 2015. Probing the core-mantle boundary beneath Europe and western Eurasia: a detailed study using PcP, *Phys. Earth planet. Inter.,* **246,** 9–24.

Hansen, S.E., Garnero, E.J., Li, M., Shim, S.-H. & Rost, S., 2023. Globally distributed subducted materials along the Earth's core-mantle boundary: implications for ultralow velocity zones, *Sci. Adv.,* **9,** 1–11.

Haugland, S.M., Ritsema, J., van Keken, P.E. & Nissen-Meyer, T., 2018. Analysis of PKP scattering using mantle mixing simulations and axisymmetric 3D waveforms, *Phys. Earth planet. Inter.,* **276,** 226–233.

Havens, E. & Revenaugh, J., 2001. A broadband seismic study of the lowermost mantle beneath Mexico: constraints on ultralow velocity zone elasticity and density, *J. geophys. Res.,* **106,** 30 809–30 820.

He, Y. & Wen, L., 2009. Structural features and shear-velocity structure of the "Pacific Anomaly," *J. geophys. Res.,* **114,** doi:10.1029/2008JB005814.

Helmberger, D.V., Wen, L. & Ding, X., 1998. Seismic evidence that the source of the Iceland hotspot lies at the core-mantle boundary, *Nature,* **396,** 251–255.

Jahnke, G., Thorne, M.S., Cochard, A. & Igel, H., 2008. Global SH-wave propagation using a parallel axisymmetric spherical finite-difference scheme: application to whole mantle scattering, *Geophys. J. Int.,* **173,** 815–826.

Jenkins, J., Mousavi, S., Li, Z. & Cottaar, S., 2021. A high-resolution map of Hawaiian ULVZ morphology from ScS phases, *Earth planet. Sci. Lett.,* **563,** doi:10.1016/j.epsl.2021.116885.

Jones, T.D., Davies, D.R. & Sossi, P.A., 2019. Tungsten isotopes in mantle plumes: heads it's positive, tails it's negative, *Earth planet. Sci. Lett.,* **506,** 255–267.

Kelly, I. & Lines, L., 1994. Noise suppression for deconvolution, *Can. J. Explor. Geophys.,* **30,** 120–126.

Kim, D., Lekic, V., Menard, B., Baron, D. & Taghizadeh-Popp, M., 2020. Sequencing seismograms: a panoptic view of scattering in the core-mantle boundary region, *Science,* **368,** 1223–1228.

Ko, B., Chariton, S., Prakapenka, V., Chen, B., Garnero, E.J., Li, M. & Shim, S.-H., 2022. Water-induced diamond formation at Earth's core-mantle boundary, *Geophys. Res. Lett.,* **49,** 49. doi:10.1029/2022GL098271.

Koelemeijer, P., Ritsema, J., Deuss, A. & Van Heijst, H.-J., 2016. SP12RTS: a degree-12 model of shear- and compressional-wave velocity for Earth's mantle, *Geophys. J. Int.,* **204,** 1024–1039.

Krier, J., Thorne, M.S., Leng, K. & Nissen-Meyer, T., 2021. A compositional component to the Samoa ultralow-velocity zone revealed through 2- and 3-D waveform modeling of SKS and SKKS differential travel-times and amplitudes, *J. geophys. Res.,* **126,** 126, doi:10.1029/2021JB021897.

Labrosse, S., Hernlund, J.W. & Coltice, N., 2007. A crystallizing dense magma ocean at the base of the Earth's mantle, *Nature,* **450,** 866–869.

Lai, V.H., Helmberger, D.V., Dobrosavljevic, V.V., Wu, W., Sun, D., Jackson, J.M. & Gurnis, M., 2022. Strong ULVZ and slab interaction at the northeastern edge of the Pacific LLSVP favors plume generation, *G-cubed,* **23,** doi:10.1029/2021GC010020.

Lay, T., Hernlund, J.W., Garnero, E.J. & Thorne, M.S., 2006. A post-perovskite lens and D" heat flux beneath the Central Pacific, *Science,* **314,** 1272–1276.

Li, J., Sun, D. & Bower, D.J., 2022. Slab control on the mega-sized North Pacific ultra-low velocity zone, *Nat. Commun.,* **13,** doi:10.1038/s41467-022-28708-8.

Li, M., 2020. The formation of hot thermal anomalies in cold subduction-influenced regions of Earth's lowermost mantle, *J. geophys. Res.,* **125,** doi:10.1029/2019jb019312.

Li, M., 2023. Variable distribution of subducted oceanic crust beneath subduction regions of the lowermost mantle, *Phys. Earth planet. Inter.,* 107063, **341,** doi:10.1016/j.pepi.2023.107063.

Li, M., McNamara, A.K., Garnero, E.J. & Yu, S., 2017. Compositionally-distinct ultra-low velocity zones on Earth's core-mantle boundary, *Nat. Commun.,* **8,** 1–9.

Li, Y., Miller, M.S., Tkalčić, H. & Sambridge, M., 2021. Small-scale heterogeneity in the lowermost mantle beneath Alaska and northern Pacific revealed from shear-wave triplications, *Earth planet. Sci. Lett.,* **559,** doi:10.1016/j.epsl.2021.116768.

Liu, L., Tan, Y., Sun, D., Chen, M. & Helmberger, D.V., 2011. Trans-pacific whole mantle structure, *J. geophys. Res.,* **116,** doi:10.1029/2010JB007907.

Ma, X. *et al.*, 2016. Strong seismic scatterers near the core-mantle boundary north of the Pacific Anomaly, *Phys. Earth planet. Inter.* **253,** 21–30.

Mancinelli, N.J., Shearer, P. & Thomas, C., 2016. On the frequency dependence and spatial coherence of PKP precursor amplitudes, *J. geophys. Res.,* **121,** 1873–1889.

Manga, M. & Jeanloz, R., 1996. Implications of a metal-bearing chemical boundary layer in D" for mantle dynamics, *Geophys. Res. Lett.,* **23,** 3091–3094.

Mao, W.L. *et al.*, 2006. Iron-rich post-perovskite and the origin of ultralow-velocity zones, *Science* **312,** 564–565.

McNamara, A.K., 2019. A review of large low shear velocity provinces and ultra low velocity zones, *Tectonophysics,* **760,** 199–220.

Nomura, R., Ozawa, H., Tateno, S., Hirose, K., Hernlund, J.W., Muto, S., Ishii, H. & Hiraoka, N., 2011. Spin crossover and iron-rich silicate melt in the Earth's deep mantle, *Nature,* **473,** 199–202.

Otsuka, K. & Karato, S.-I., 2012. Deep penetration of molten iron into the mantle caused by a morphological instability, *Nature,* **492,** 243–246.

Owens, T.J., Crotwell, H.P., Groves, C. & Oliver-Paul, P., 2004. SOD: standing Order for data, *Seismol. Res. Lett.,* **75,** 515–520.

Pachhai, S., Li, M., Thorne, M.S., Dettmer, J. & Tkalčić, H., 2022a. Internal structure of ultralow-velocity zones consistent with origin from a basal magma ocean, *Nat. Geosci.,* **15,** 79–84.

Pachhai, S., Thorne, M.S. & Nissen-Meyer, T., 2022b. Quantification of small-scale heterogeneity at the core-mantle boundary using sample entropy of SKS and SPdKS synthetic waveforms, *Minerals,* **12,** 1–30.

Pachhai, S., Thorne, M.S. & Rost, S., 2023. Improved characterization of ultralow-velocity zones through advances in bayesian inference of ScP waveforms, *J. geophys. Res.,* **128,** 128, doi:10.1029/2023JB026415.

Pachhai, S., Thorne, M.S. & Rost, S., 2024. Examining the influence of 2.5-D ultra-low velocity zone morphology on ScP waveforms and estimated elastic parameters, *Geophys. J. Int.,* **239,** 591–620.

Pachhai, S., Tkalčić, H. & Dettmer, J., 2014. Bayesian inference for ultralow velocity zones in the Earth's lowermost mantle: complex ULVZ beneath the east of the Philippines, *J. geophys. Res.,* **119,** 8346–8365.

Pradhan, G.K., Fiquet, G., Siebert, J., Auzende, A.-L., Morard, G., Antonangeli, D. & Garbarino, G., 2015. Melting of MORB at core-mantle boundary, *Earth planet. Sci. Lett.,* **431,** 247–255.

Ritsema, J., Deuss, A., van Heijst, H.-J. & Woodhouse, J.H., 2011. S40RTS: a degree-40 shear-velocity model for the mantle from new Rayleigh wave dispersion, teleseismic traveltime and normal-mode splitting function measurements, *Geophys. J. Int.,* **184,** 1223–1236.

Robinson, J.C., 1970. Statistically optimal stacking of seismic data, *Geophysics,* **35,** 436–446.

Rost, S., Garnero, E.J. & Williams, Q., 2006. Fine-scale ultralow-velocity zone structure from high-frequency seismic array data, *J. geophys. Res.,* **111,** doi:10.1029/2005JB004088.

Rost, S., Garnero, E.J., Williams, Q. & Manga, M., 2005. Seismological constraints on a possible plume root at the core-mantle boundary, *Nature,* **435,** 666–669.

Rost, S. & Revenaugh, J., 2001. Seismic detection of rigid zones at the top of the core, *Science,* **294,** 1911–1914.

Rost, S. & Revenaugh, J., 2003. Small-scale ultralow-velocity zone structure imaged by ScP, *J. geophys. Res.,* **108,** doi:10.1029/2001JB001627.

Rost, S. & Thomas, C., 2009. Improving seismic resolution through array processing techniques, *Surv. Geophys.,* **30,** 271–299.

Rost, S. & Thomas, C., 2010. High resolution CMB imaging from migration of short-period core reflected phases, *Phys. Earth planet. Inter.,* **183,** 143–150.

Sidorin, I., Gurnis, M. & Helmberger, D.V., 1999. Evidence for a ubiquitous seismic discontinuity at the base of the mantle, *Science,* **286 ,** 1326–1331.

Sun, D., Helmberger, D.V., Lai, V.H., Gurnis, M., Jackson, J.M. & Yang, H.-Y., 2019. Slab control on the northeastern edge of the mid-Pacific LLSVP near Hawaii, *Geophys. Res. Lett.,* **46,** 3142–3152.

Takeuchi, N. & Obara, K., 2010. Fine-scale topography of the D" discontinuity and its correlation to volumetric velocity fluctuations, *Phys. Earth planet. Inter.,* **183,** 126–135.

Tan, E., Gurnis, M. & Han, L., 2002. Slabs in the lower mantle and their modulation of plume formation, *G-cubed,* **3,** 1–24.

Thorne, M.S., Crotwell, H.P. & Jahnke, G., 2013a. An educational resource for visualizing the global seismic wavefield, *Seismol. Res. Lett.,* **84,** 711–717.

Thorne, M.S. & Garnero, E.J., 2004. Inferences on ultralow-velocity zone structure from a global analysis of SPdKS waves, *J. geophys. Res.,* **109,** doi:10.1029/2004JB003010.

Thorne, M.S., Lay, T., Garnero, E.J., Jahnke, G. & Igel, H., 2007. Seismic imaging of the laterally varying D" region beneath the Cocos Plate, *Geophys. J. Int.,* **170,** 635–648.

Thorne, M.S., Leng, K., Pachhai, S., Rost, S., Wicks, C.W. & Nissen-Meyer, T., 2021. The most parsimonious ultralow-velocity zone distribution from highly anomalous SPdKS waveforms, *G-cubed,* **22,** doi:10.1029/2020GC009467.

Thorne, M.S., Pachhai, S., Leng, K., Wicks, J.K. & Nissen-Meyer, T., 2020. New candidate ultralow-velocity zone locations from highly anomalous SPdKS waveforms, *Minerals,* **10,** 211, 1–26.

Thorne, M.S., Takeuchi, N. & Shiomi, K., 2019. Melting at the edge of a slab in the deepest mantle, *Geophys. Res. Lett.,* **46,** 8000–8008.

Thorne, M.S., Zhang, Y. & Ritsema, J., 2013b. Evaluation of 1D and 3D seismic models of the Pacific lower mantle with S, SKS, and SKKS traveltimes and amplitudes, *J. geophys. Res.,* **118,** 985–995.

Thybo, H., Ross, A.R. & Egorkin, A.V., 2003. Explosion seismic reflections from the Earth's core, *Earth planet. Sci. Lett.,* **216,** 693–702.

Wessel, P., Luis, J.F., Uieda, L., Scharroo, R., Wobbe, F., Smith, W.H.F. & Tian, D., 2019. The generic mapping tools version 6, *G-cubed,* **20,** 5556–5564.

Whittaker, S., Thorne, M.S., Schmerr, N.C. & Miyagi, L., 2016. Seismic array constraints on the D" discontinuity beneath Central America, *J. geophys. Res.,* **120,** 1–18.

Widess, M.B., 1973. How thin is a thin bed?, *Geophysics,* **38,** 1176–1180.

Williams, Q., Revenaugh, J. & Garnero, E.J., 1998. A correlation between ultra-low basal velocities in the mantle and hot spots, *Science,* **281,** 546–549.

Wolf, J. & Long, M.D., 2023. Lowermost mantle structure beneath the Central Pacific Ocean: ultralow velocity zones and seismic anisotropy, *G-cubed,* **24,** doi:10.1029/2022GC010853.

Wolf, J., Long, M.D. & Frost, D.A., 2024. Ultralow velocity zone and deep mantle flow beneath the Himalayas linked to subducted slab, *Nat. Geosci.,***17,** 302–308.

Yao, Y., Whittaker, S. & Thorne, M.S., 2015. D″ discontinuity structure beneath the North Atlantic from *Scd* observations, *Geophys. Res. Lett.,* **42,** 1–9.

Yu, S., 2020. Extreme Seismic Anomalies near Earth's Core Mantle Boundary, *PhD dissertation*, Arizona State University.

Yu, S. & Garnero, E.J., 2018. Ultralow velocity zone locations: a global assessment, *G-cubed,* **19,** 396–414.

Yuan, K. & Romanowicz, B., 2017. Seismic evidence for partial melting at the root of major hot spot plumes, *Science,* **357,** 393–397.

Zhao, C., Garnero, E.J., Li, M., McNamara, A. & Yu, S., 2017. Intermittent and lateral varying ULVZ structure at the northeastern margin of the Pacific LLSVP, *J. geophys. Res.,* **122,** 1198–1220.